

**ANALYSIS OF PRESSURE DATA OBTAINED AT TRANSONIC  
SPEEDS ON A THIN LOW-ASPECT-RATIO CAMBERED  
DELTA WING-BODY COMBINATION**

By

John P. <sup>Philip</sup>Mugler, Jr.

Thesis submitted to the Graduate Faculty of the  
Virginia Polytechnic Institute  
in candidacy for the degree of  
**MASTER OF SCIENCE**  
in  
Aeronautical Engineering

APPROVED:

APPROVED:

---

Director of Graduate Studies

---

Head of Department

---

Dean of Engineering

---

Supervisor

May 1958

Blacksburg, Virginia

~~CONFIDENTIAL~~

TABLE OF CONTENTS

	Page
I. LIST OF FIGURES . . . . .	3
II. INTRODUCTION . . . . .	5
III. LIST OF SYMBOLS . . . . .	6
IV. APPARATUS . . . . .	9
V. TESTS . . . . .	17
VI. MEASUREMENTS AND ACCURACY . . . . .	20
VII. CORRECTIONS . . . . .	23
VIII. DATA REDUCTION . . . . .	24
IX. THEORETICAL CONSIDERATIONS . . . . .	29
X. RESULTS AND DISCUSSION . . . . .	31
XI. CONCLUSIONS . . . . .	58
XII. SUMMARY . . . . .	59
XIII. ACKNOWLEDGEMENTS . . . . .	60
XIV. REFERENCES . . . . .	61
XV. VITA . . . . .	63

CONFIDENTIAL

I. LIST OF FIGURES

Figure	Page
1. Model Details	
(a) Wing-Body Combinations . . . . .	14
(b) Details of Leading-Edge Camber . . . . .	15
(c) Photograph of Basic Pressure Wing-Body Combination . . . . .	18
(d) Photograph of Indented Pressure Wing-Body Combination . . . . .	19
2. Location of Pressure Orifices. . . . .	21
3. Spanwise Load Distributions	
(a) $M = 0.60$ and $0.80$ . . . . .	32
(b) $M = 0.90$ and $0.94$ . . . . .	33
(c) $M = 0.98$ and $1.03$ . . . . .	34
(d) $M = 1.12$ and $1.43$ . . . . .	35
4. Aerodynamic Characteristics of the Wing in the Presence of the Body	
(a) $\alpha$ Versus $C_{N,w}$ . . . . .	37
(b) $C_{m,w}$ Versus $C_{N,w}$ . . . . .	38
(c) $C_{B,w}$ Versus $C_{N,w}$ . . . . .	39
5. Aerodynamic Characteristics of the Basic and Indented Bodies in the Presence of the Wing . . . . .	40
6. Aerodynamic Characteristics of the Basic Wing-Body Combination	
(a) $C_N$ Versus $\alpha$ . . . . .	41
(b) $C_m$ Versus $C_N$ . . . . .	42

Figure	Page
7. Aerodynamic Characteristics of the Indented Wing-Body	
Combination	
(a) $C_N$ Versus $\alpha$ . . . . .	43
(b) $C_m$ Versus $C_N$ . . . . .	44
8. Variation of Longitudinal and Lateral Location of Center of Pressure	
(a) Variation With Mach Number . . . . .	46
(b) Variation With Wing Normal-Force Coefficient . . . . .	47
9. Division of Normal Load . . . . .	49
10. Comparison of Pressure Distributions for the Plane and Cambered Wings	
(a) $M = 0.80$ . . . . .	51
(b) $M = 1.03$ . . . . .	53
11. Comparison of Span Loading Characteristics for Plane and Cambered Wings . . . . .	55
12. Comparison of Theoretical and Experimental Results . . . . .	56

CONFIDENTIAL

- 5 -

## II. INTRODUCTION

It has been realized that, theoretically, the low-aspect ratio flat delta wing with full leading-edge suction approaches minimum induced drag (see ref. 1). In the past, much research effort has been expended to investigate the feasibility of utilizing a wing of this general plan form for high-speed flight and thus take advantage of the lower induced drag characteristics (see refs. 2, 3, 4, and 5, for example). Experiment indicates that unless the leading-edge portion of the wing is properly cambered, leading-edge flow separation will cause the loss of the beneficial leading-edge suction. Force tests of several types of leading-edge modifications have shown conical camber to be rather effective in utilizing this beneficial suction force to lower the induced drag (see ref. 2). Flight tests of the YF-102 airplane verified this finding (ref. 6). Therefore, pressure tests of a conical cambered wing configuration have been made to investigate the aerodynamic loading characteristics. The basic pressure measurements, without analysis, are presented in reference 7. The present paper will analyze these data.

CONFIDENTIAL

CONFIDENTIAL

- 6 -

III. LIST OF SYMBOLS

Any consistent set of units may be used:

- b wing span (to rounded tips, see Fig. 1)
- $b'/2$  unsupported semispan (distance from wing-body juncture to rounded wing tip)
- c airfoil section chord, measured parallel to plane of symmetry
- $\bar{c}$  wing mean aerodynamic chord,  $\frac{2}{S} \int_0^{b/2} c^2 dy$
- $c_{av}$  wing average chord,  $\frac{\text{root chord} + \text{tip chord}}{2}$
- $C_m(c/4)$  wing section pitching-moment coefficient about  $0.25c$
- $C_n$  wing section normal-force coefficient
- $C_m(\bar{c}/4)$  wing section pitching-moment coefficient about  $0.25\bar{c}$
- $C_{B,w}$  wing bending-moment coefficient about body center line
- $C_m$  wing-body pitching-moment coefficient about  $0.25\bar{c}$
- $C_{m,fv}$  body pitching-moment coefficient about  $0.25\bar{c}$ , based on wing area and  $\bar{c}$
- $C_{m,w}$  wing pitching-moment coefficient about  $0.25\bar{c}$
- $C_N$  wing-body normal-force coefficient
- $C_{N,fv}$  body normal-force coefficient based on wing area
- $C_{N,w}$  wing normal-force coefficient
- $C_p$  pressure coefficient
- $D_{max}$  maximum body diameter

CONFIDENTIAL

CONFIDENTIAL

- 7 -

$l$	body length
$M$	free-stream Mach number
$p$	local static pressure
$q$	free-stream dynamic pressure
$r$	body radius at any station
$\bar{r}$	root-mean-square body radius taken between wing-body leading-edge and trailing-edge junctures
$r_{\max}$	maximum body radius
$S$	wing area
$x$	distance measured streamwise from section leading edge or from body nose
$y$	distance measured laterally from plane of symmetry
$y'$	distance measured laterally from wing-body juncture
$Y$	vertical distance from wing chord plane of uncambered section to upper or lower surface
$Z$	vertical displacement of wing leading edge
$\alpha$	angle of attack of body center line
$\Delta\alpha$	angle of twist between wing chord and body center line
$\theta$	meridian angle of body orifice station
$\frac{\partial\Delta\alpha}{\partial m}$	wing-twist influence coefficient due to moment about quarter-chord line
$\frac{\partial\Delta\alpha}{\partial n}$	wing-twist influence coefficient due to normal load at quarter-chord point

CONFIDENTIAL

Subscripts:

e	exposed
cp	center of pressure
i	index denoting spanwise position
j	index of summation over span
L	lower surface
max	maximum
U	upper surface



CONFIDENTIAL

- 9 -

#### IV. APPARATUS

##### Tunnels

The pressure data at subsonic and transonic speeds were obtained in the Langley 8-foot transonic tunnel. This facility is a single-return, atmospheric type wind tunnel with cooling accomplished by means of air exchange with the outside atmosphere. Details of the tunnel along with a calibration of the slotted test section are presented in reference 8.

The fan section of the tunnel is made up of two tandem rotors having 17 fixed-pitch blades in each rotor. Prerotation vanes upstream direct the air into the rotors and counterrotation vanes downstream reduce the rotation of the air mass leaving the fans. The two rotors are mounted on the same shaft and are driven by a 22,000-horsepower motor. The motor speed is variable from 0 to 990 rpm.

The test section of the 8-foot transonic tunnel is do-decagonal in cross section and has a cross-sectional area of 42.64 sq ft at the minimum section. Longitudinal slots are located between each of the 12 wall panels (see Fig. 1, ref. 8) to allow continuous operation through the transonic speed range with negligible effects of choking and blockage. The slots contain about 11 percent of the total periphery of the test section. Six of the 12 wall panels have windows to allow for schlieren observations. The entire test section is enclosed in a hemispherical chamber.

CONFIDENTIAL

CONFIDENTIAL

- 10 -

The Mach number in the test section can be continuously varied from 0 to 1.2, the higher value being somewhat dependent on model size. The Mach number distribution, with a survey tube mounted in the test section, is reasonably uniform throughout the test region length of about 3 feet (see Fig. 7, ref. 8). Local deviations from the average stream Mach number were about  $\pm 0.003$  at subsonic speeds. With increases in Mach number, these deviations increased but did not exceed  $\pm 0.010$  at a Mach number of 1.2.

The stagnation temperature of the tunnel air can be controlled by vanes and blocks in the air exchange tower. Generally stagnation temperatures around  $150^{\circ}$  F are maintained. The maximum stagnation temperature permissible is  $180^{\circ}$  F, this limit being imposed because of the tunnel equipment. The test Reynolds number is about  $3.5$  to  $4 \times 10^6$  per foot at the higher Mach numbers.

During the present investigation the model was mounted in the tunnel on a support tube which in turn was fixed axially in the center of the tunnel by two sets of support struts projecting from the tunnel walls (see Fig. 1, ref. 8). The forward portion of the support tube was tapered and fitted to the tapered sting extending from the base of the model. This tapered portion of the support tube was hinged to the rear portion in such a manner that angle-of-attack changes could be accomplished by means of an electric motor driving an actuating screw located within the tube. This mechanism was controlled remotely and therefore permitted angle changes with the tunnel operating. A series of angular couplings

CONFIDENTIAL

CONFIDENTIAL

- 11 -

are provided which fit between the model sting and the tapered portion of the support tube. These couplings are designed so as to keep the model near the center line of the tunnel at all angles of attack.

The pressure data at a Mach number of 1.43 were obtained in the Langley 8-foot transonic pressure tunnel. This facility is a single-return, closed-circuit, pressure tunnel capable of operating at atmospheric stagnation pressure and below. The calibration report for this facility containing the details of the flow characteristics and descriptions of the pertinent items is not yet published. However, a brief description of the test section and some representative Mach number distributions at the center of the test section have been presented in reference 3.

The tunnel fan section is composed of a single rotor followed immediately downstream by two sets of 23 straightening vanes. The rotor is about 17 feet in diameter and has 32 wooden blades. Power to the fan is furnished by a 25,000-horsepower motor with speed control to 840 rpm. Test section Mach number is maintained by controlling the speed of the drive motor.

The tunnel air temperature is controlled by finned cooling coils across one corner of the tunnel. Water is circulated through the cooling coils and then pumped to a cooling tower where it is cooled by the atmosphere. During this investigation the stagnation temperature was automatically controlled and was kept constant and uniform across the

CONFIDENTIAL

CONFIDENTIAL

- 12 -

tunnel at 120° F. The tunnel air can also be dried to a dewpoint of about -40° F by circulating it through a dryer using silica gel as a desiccant. During this investigation the dewpoint was controlled and kept at about 0° F.

The test section of the 8-foot transonic pressure tunnel is rectangular in cross section and has a cross-sectional area of 50.90 sq ft at the minimum section. The upper and lower walls of the test section are slotted longitudinally to permit continuous operation through the transonic speed range (see Fig. 1, ref. 3). The slots comprise about 5 percent of the total periphery of the test section. The slots can be enclosed with specially designed channels which converts the slotted test section into a supersonic nozzle. This tunnel configuration was used for the present investigation. Details of the nozzle shape and the test-section Mach number distribution are presented in reference 9. With a survey tube mounted in the test section, local deviations from the average free-stream Mach number did not exceed  $\pm 0.015$  throughout the test region length of about 3 feet.

The stagnation pressure of the tunnel can be varied continuously from 1/4 to 1.0 atmosphere. This affords a test Reynolds number range from 1 to  $4 \times 10^6$  per foot.

The sting-type model support system was utilized for these tests. The sting was attached to a tapered support strut which in turn was connected downstream to a motor-driven metal arc. The system is designed

CONFIDENTIAL

CONFIDENTIAL

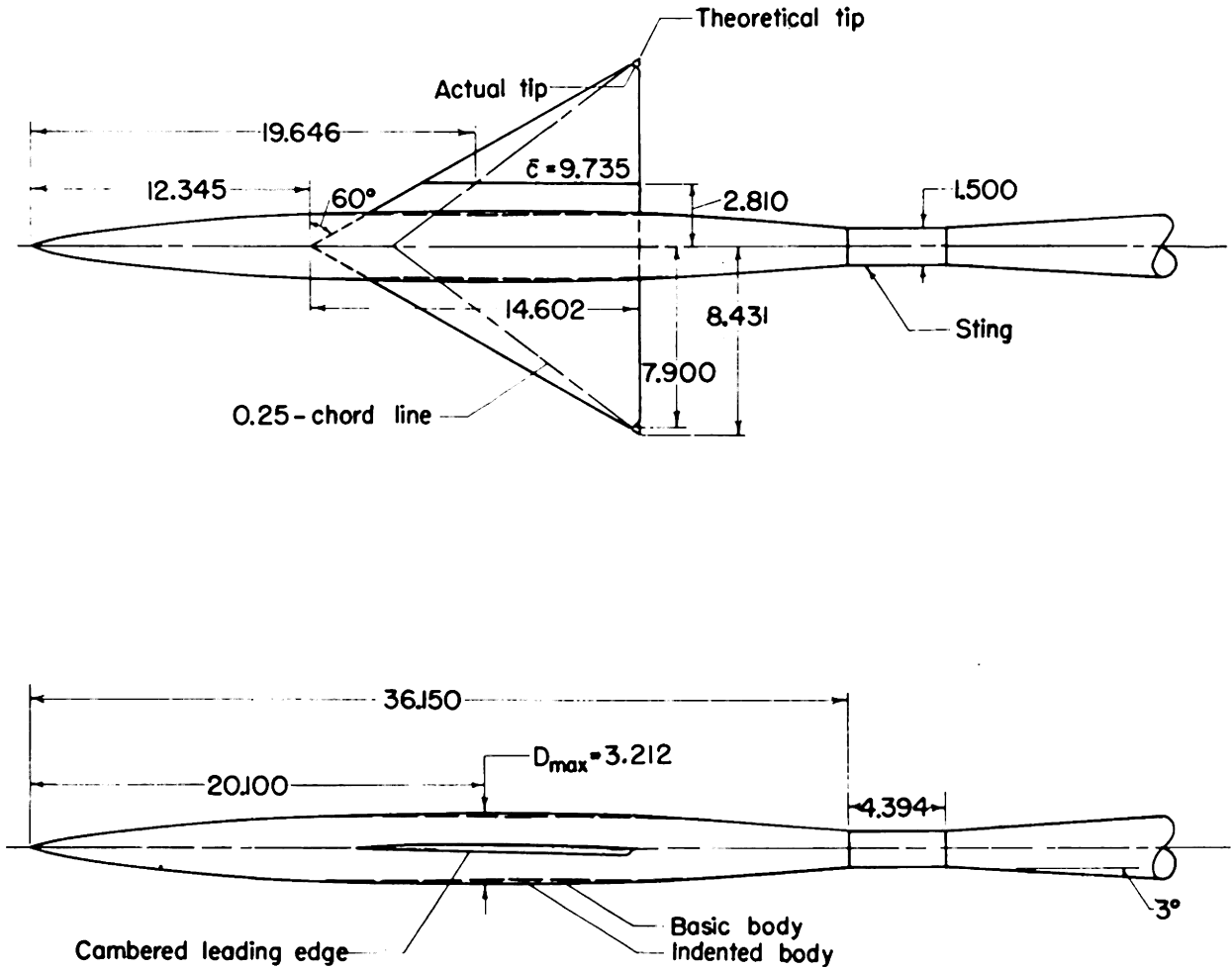
- 13 -

so as to keep the center of gravity of the model near the center line of the test section over an angle-of-attack range from  $-10^{\circ}$  to  $+15^{\circ}$ . For angles of attack outside this range, a series of angular couplings are provided. The angle-of-attack mechanism is remotely controlled during the tests.

Models

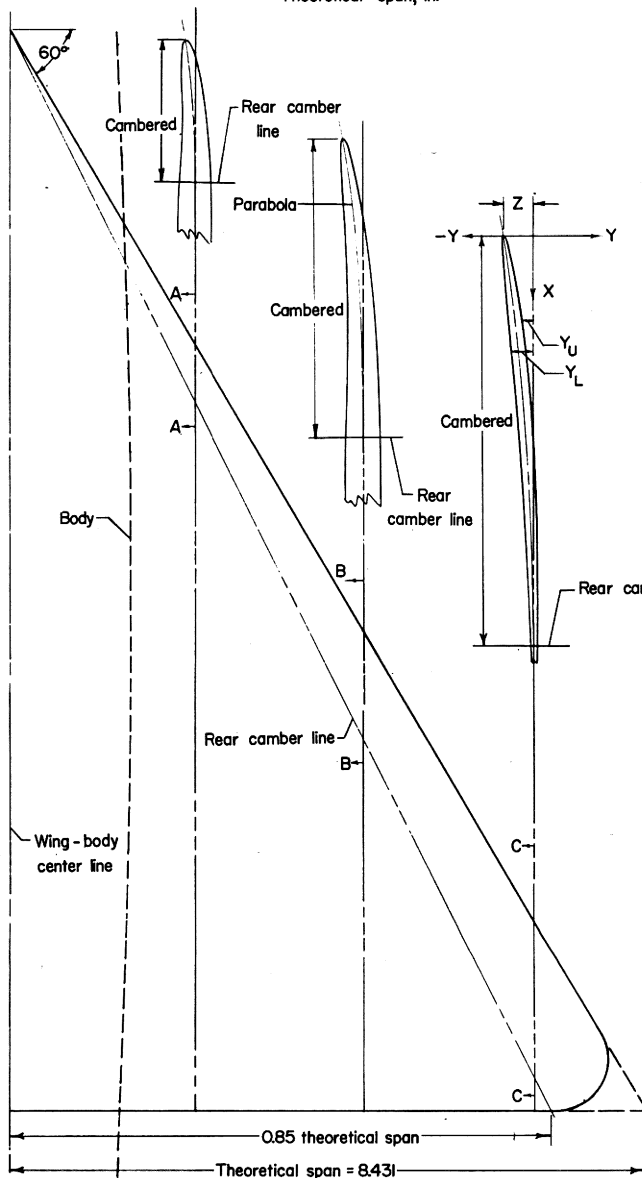
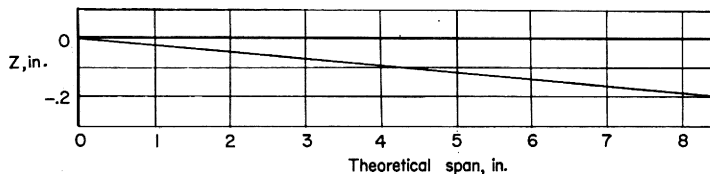
The delta wing used in this investigation has  $60^{\circ}$  sweepback of the leading edge, a taper ratio of 0, and NACA 65A003 airfoil sections parallel to the model plane of symmetry over the uncambered portion of the wing (see Fig. 1(a)). The leading-edge portion of the wing has conical camber over the outboard 15 percent of each semispan. Conical camber denotes that the surface is conical with respect to the wing apex and the surface trace will be similar irrespective of the location of a viewing plane perpendicular to the  $x$  axis. This camber was designed for a lift coefficient of 0.15 near  $M = 1.0$ . The amount of the leading-edge line vertical displacement at any spanwise station was obtained utilizing references 10 and 11. Then a parabolic mean camber line was fitted in the streamwise direction between the displaced leading edge and a line at 85 percent of the local semispan. Next, the thickness distribution of the plane wing was sheared vertically until it was distributed evenly about the parabolic mean line. Details of this modification are shown in Figure 1(b). The actual wing plan form deviated from the theoretical delta wing plan form in that the wing tips were rounded (see Fig. 1(a)). Rounding the tips reduced the wing area by a small

CONFIDENTIAL



(a) Wing-body combinations.

Figure 1.- Model details. All dimensions in inches unless otherwise noted.



SECTION A-A			
X <sub>U</sub>	Y <sub>U</sub>	X <sub>L</sub>	Y <sub>L</sub>
0	-0.056	0	-0.056
0.011	-0.043	0.015	-0.066
0.024	-0.035	0.028	-0.069
0.036	-0.029	0.042	-0.071
0.049	-0.024	0.055	-0.073
0.074	-0.016	0.082	-0.074
0.125	-0.001	0.135	-0.076
0.255	0.027	0.265	-0.075
0.516	0.063	0.523	-0.073
0.648	0.075	0.651	-0.077

L. E. Rad. = 0.006

SECTION B-B			
X <sub>U</sub>	Y <sub>U</sub>	X <sub>L</sub>	Y <sub>L</sub>
0	-0.108	0	-0.108
0.007	-0.100	0.009	-0.111
0.015	-0.095	0.018	-0.116
0.023	-0.091	0.026	-0.117
0.030	-0.088	0.035	-0.118
0.046	-0.083	0.051	-0.119
0.078	-0.073	0.085	-0.119
0.158	-0.053	0.167	-0.117
0.320	-0.022	0.330	-0.107
0.482	0.005	0.492	-0.098
0.645	0.021	0.654	-0.091
0.971	0.060	0.978	-0.082
1.298	0.080	1.300	-0.082

L. E. Rad. = 0.004

SECTION C-C			
X <sub>U</sub>	Y <sub>U</sub>	X <sub>L</sub>	Y <sub>L</sub>
0	-0.160	0	-0.160
0.003	-0.157	0.004	-0.162
0.006	-0.155	0.007	-0.163
0.009	-0.153	0.011	-0.164
0.012	-0.152	0.014	-0.164
0.018	-0.150	0.021	-0.164
0.031	-0.146	0.034	-0.164
0.063	-0.137	0.067	-0.163
0.128	-0.124	0.132	-0.158
0.191	-0.111	0.197	-0.152
0.257	-0.100	0.263	-0.147
0.386	-0.078	0.393	-0.135
0.516	-0.059	0.523	-0.123
0.646	-0.042	0.653	-0.112
0.776	-0.027	0.783	-0.101
0.906	-0.014	0.913	-0.090
1.037	-0.003	1.043	-0.080
1.167	0.007	1.172	-0.071
1.297	0.014	1.302	-0.062
1.428	0.020	1.431	-0.053
1.558	0.023	1.561	-0.045
1.688	0.024	1.690	-0.038
1.819	0.024	1.820	-0.031
1.949	0.022	1.949	-0.024
2.079	0.019	2.079	-0.019

L. E. Rad. = 0.002

(b) Details of leading-edge camber. Plan form and streamwise airfoil sections are not to same scale.

Figure 1.- Continued.

CONFIDENTIAL

- 16 -

amount (a reduction of 0.6 percent of the total wing area of 0.855 sq ft) and produced negligible changes in mean aerodynamic chord length and location. The theoretical aspect ratio, which assumes pointed tips, is 2.31. The wing was constructed of steel and was tested as a midwing configuration.

The wing was tested in combination with basic and indented bodies. The basic body is a body of revolution designed to have minimum wave drag for a given length and volume. Generally, this is designated a Sears-Haack body and its shape can be expressed by the equation for the radius of the body as

$$r = r_{\max} \left[ 1 - \left( 1 - \frac{2x}{L} \right)^2 \right]^{3/2}$$

In this equation,  $L$  represents the length of the body for complete closure at the aft end. The necessity for providing an opening at the aft end of the body to accommodate the sting support required that the actual body length be less. For this configuration the actual body length was about 90 percent of the length for complete closure.

The indented body was a body of revolution indented symmetrically for a Mach number of 1.2 in accordance with the supersonic area-rule concept (ref. 12). Ordinates for both the basic and indented bodies are presented in reference 7.

CONFIDENTIAL



CONFIDENTIAL

- 17 -

V. TESTS

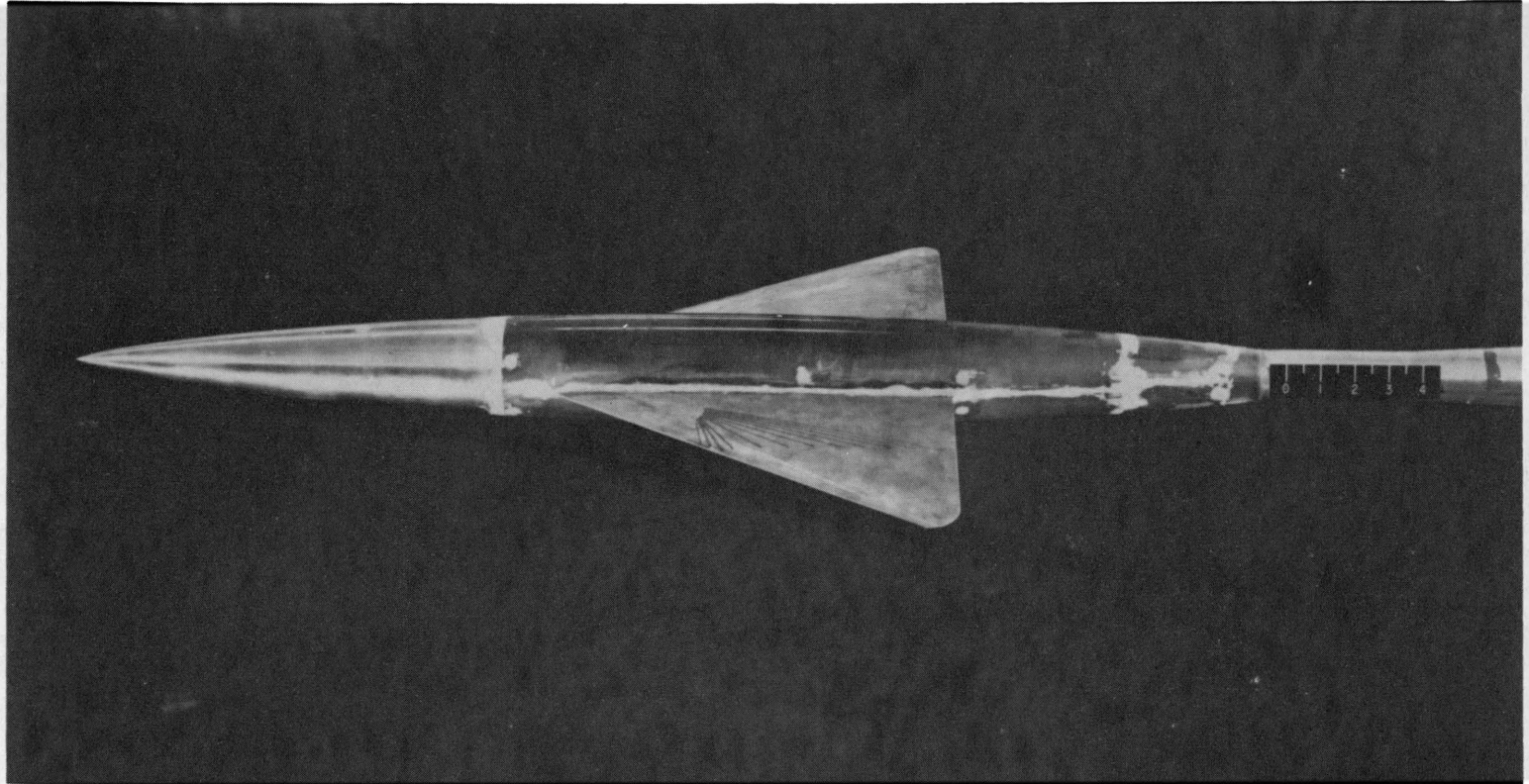
For this investigation a pressure wing was tested in combination with both a basic body of revolution and an indented body (see Figs. 1(c) and 1(d) for photographs of models). Both configurations were tested at Mach numbers from 0.60 to 1.12 and at a Mach number of 1.43. Generally the angle-of-attack range extended from  $-4^{\circ}$  to  $20^{\circ}$ . However at  $M = 1.43$  the angle-of-attack measuring device did not function properly and the resultant angles deviated from the values used at the other Mach numbers. Also, at  $M = 1.43$  data for the indented body configuration were not obtained for the two highest angles of attack.

The Reynolds number, based on the wing mean aerodynamic chord, varied during the tests from about  $2.8 \times 10^6$  at a Mach number of 0.60 to  $3.3 \times 10^6$  at the highest test Mach number of 1.43. The free-stream dynamic pressure varied from about 400 to 900 pounds per square foot over the same Mach number range.

To insure turbulent boundary layer on the model, transition strips were fixed on both configurations during all the tests. The strips were about 0.10 inch wide and were formed by sprinkling No. 120 carborundum grains on a plastic adhesive. The strips extended from the wing-body juncture to the wing tip at 10 percent of the local chord on the upper and lower wing surfaces and formed a ring around the body at 10 percent of the body length.

CONFIDENTIAL

CONFIDENTIAL



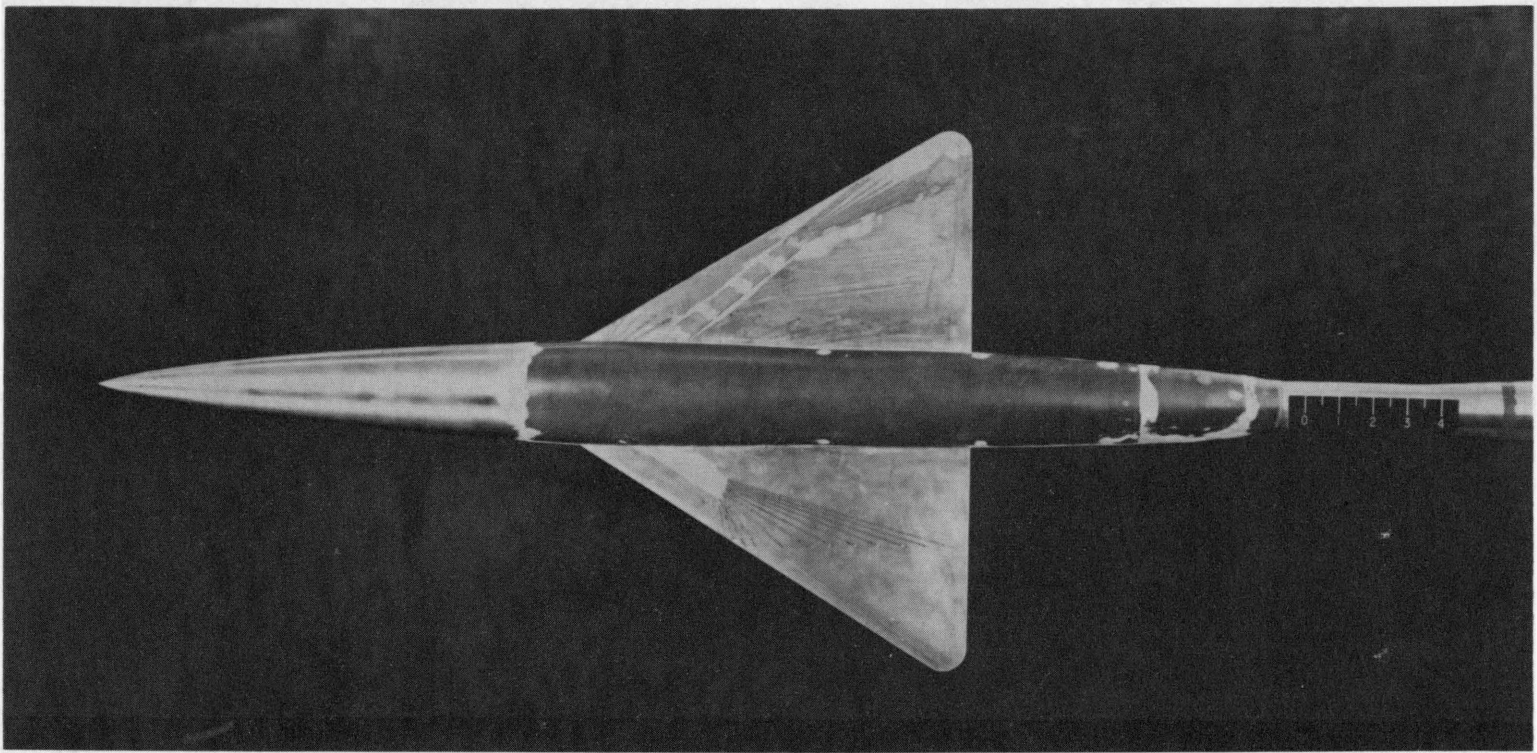
- 18 -

CONFIDENTIAL

(c) Photograph of basic pressure wing-body combination. <sup>L-89613</sup>

Figure 1.- Continued.

CONFIDENTIAL



- 19 -

CONFIDENTIAL

(d) Photograph of indented pressure wing-body combination. L-89620

Figure 1.- Concluded.

CONFIDENTIAL

- 20 -

VI. MEASUREMENTS AND ACCURACY

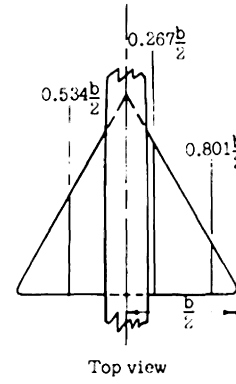
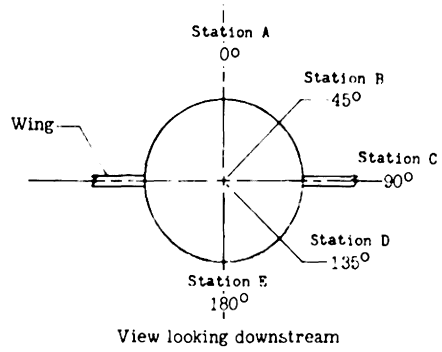
Measurements of the local static pressure on the models were made by using about 139 flush-mounted orifices distributed over the upper and lower wing surfaces at three wing semispan locations and along five body meridian rows (see Fig. 2). Each of these orifices was in turn connected to multitube manometer boards using flexible tubing. At each data point the pressures on both the wing and the body were recorded simultaneously by photographing the manometer boards. The pressure coefficient at each orifice was computed using this photographic record and the accuracy of these measurements in coefficient form is estimated to be within  $\pm 0.005$ .

The angle of attack of the model was measured by means of a strain-gage attitude transmitter mounted in the nose of the model. A study of the factors affecting the accuracy of the results indicates that the measured angle of attack is accurate to within  $\pm 0.1^\circ$ .

The flow Mach number was obtained by relating simultaneously measured values of the stream total pressure and the local static pressures. The accuracy of these measurements is estimated to be  $\pm 0.003$  at subsonic speeds and  $\pm 0.005$  at transonic and supersonic speeds.

The model wing was calibrated statically for deflection due to load by using an arrangement of a hydraulic jack and a balance scale to apply loads at various points on the wing, in conjunction with an optical device to read vertical deflections at several stations on the wing.

CONFIDENTIAL



Location of body pressure orifices, $\frac{x}{l}$				
Meridian, 0, deg	Meridian, 45, deg	Meridian, 90, deg	Meridian, 135, deg	Meridian, 180, deg
0.055	0.166	0.055	0.166	0.055
.166	.277	.166	.277	.166
.277	.367	.277	.367	.277
.367	.387	.353	.367	.367
.387	.443	.367	.443	.387
.415	.498	.747*	.498	.443
.443	.553	.775	.553	.498
.498	.609	.830	.609	.553
.553	.664	.871	.664	.609
.581	.719	.954	.719	.664
.609	.775		.775	.719
.636	.830		.830	.775
.664	.871		.871	.830
.692				.871
.719				.954
.747				
.775				
.830				
.871				
.954				

\*Indented body only

(a) On basic and indented body.

Location of wing pressure orifices, $\frac{x}{c}$					
$0.267\frac{b}{2}$		$0.534\frac{b}{2}$		$0.801\frac{b}{2}$	
Upper surface	Lower surface	Upper surface	Lower surface	Upper surface	Lower surface
0.010	0.025	0.010	0.025	0.030	0.045
.030	.060	.030	.060	.060	.150
.060	.100	.060	.100	.100	.250
.100	.150	.100	.200	.200	.350
.150	.200	.200	.300	.300	.450
.200	.300	.300	.400	.400	.550
.300	.400	.400	.500	.500	.650
.400	.500	.500	.600	.600	.750
.500	.600	.600	.700	.700	
.600	.700	.700	.800	.850	
.700	.800	.800	.850		
.800	.850	.900			
.900	.925				
.950					

(b) On wing.

Figure 2.- Location of pressure orifices.

CONFIDENTIAL

- 22 -

The influence coefficients for the wing were obtained using these measurements. Wing-twist angles were computed at several stations on the wing by using the experimental wing section data in conjunction with these influence coefficients as follows:

$$(\Delta\alpha)_1 = q \frac{b'}{2} \int_0^1 \left[ \left( \frac{\partial \Delta\alpha}{\partial n} \right)_{1j} (cc_n)_j + \left( \frac{\partial \Delta\alpha}{\partial m} \right)_{1j} (c^2 c_m)_j \right] d\left(\frac{y'}{b'/2}\right)$$

In this equation  $j$  is the index for summation over  $\frac{y'}{b'/2}$  and takes on values of 0.142, 0.428, and 0.715 for this wing. The subscript  $i$  denotes the spanwise station where  $\Delta\alpha$  is to be calculated and for this wing  $i$  takes on values of  $\frac{2y}{b} = 0.267, 0.534, \text{ and } 0.801$ . The values of  $\left( \frac{\partial \Delta\alpha}{\partial n} \right)_{1j}$  and  $\left( \frac{\partial \Delta\alpha}{\partial m} \right)_{1j}$  are presented in Table I, reference 7;  $(cc_n)_j$  and  $(c^2 c_m)_j$  are obtained from the experimental data.

The twist angles computed in this manner are estimated to be accurate to within one-quarter of a degree.

CONFIDENTIAL

CONFIDENTIAL

- 23 -

## VII. CORRECTIONS

The axially slotted test section minimized boundary interference due to solid blockage, and a qualitative analysis indicated that other subsonic boundary interference effects on the data presented herein were either negligible or very small up to the highest angles of attack tested. At Mach numbers above 1.0 boundary interference effects consisted of shocks and expansions from the model which were reflected back to the surface of the model by the test-section boundary. At Mach numbers between 1.0 and 1.03 the boundary reflected disturbances were not of sufficient strength to affect the data. From the geometry of the test-section it was estimated that the boundary reflected disturbances passed downstream of the model at  $M = 1.12$ . This was verified by schlieren observations during the tests. Therefore no data was recorded at  $1.03 < M < 1.12$ .

The bending of a swept wing introduces effective twist which changes the loading characteristics. Twist is also introduced if the center of pressure does not lie on the elastic axis. No corrections have been applied to any of the data to account for these aeroelastic effects. In order to provide an indication of the magnitude of these effects, some of the aeroelastic twist characteristics have been calculated and presented in reference 7.

CONFIDENTIAL

CONFIDENTIAL

- 24 -

VIII. DATA REDUCTION

As previously mentioned in the measurements and accuracy section approximately 139 pressure orifices were located on the wings at three constant span stations and on the body along five longitudinal rows. The following equations and techniques were used to obtain the significant loading parameters from the measured surface pressures:

Wing Section Loads

The normal force per unit width on a wing section is

$$n = c_n qc = \int_0^c (P_L - P_U) dx$$

and

$$\begin{aligned} c_n &= \frac{n}{qc} = \frac{1}{qc} \int_0^c (P_L - P_U) dx \\ &= \frac{1}{c} \int_0^c (C_{p,L} - C_{p,U}) dx \\ &= \int_0^1 (C_{p,L} - C_{p,U}) d\left(\frac{x}{c}\right) \end{aligned} \quad (1)$$

The pitching moment per unit width on a wing section about the section quarter chord is (nose up moment is positive)

$$m_{c/4} = c_{m(c/4)} qc^2 = \int_0^c (P_L - P_U) (c/4 - x) dx$$

CONFIDENTIAL



CONFIDENTIAL

- 25 -

and

$$\begin{aligned}
 c_{m(c/4)} &= \frac{m_{c/4}}{qc^2} = \frac{1}{qc^2} \int_0^c (P_L - P_U)(c/4 - x) dx \\
 &= \int_0^1 (C_{p,L} - C_{p,U})(0.25 - x/c) d(x/c) \quad (2)
 \end{aligned}$$

The integrals of equations (1) and (2) above were evaluated by plotting the pressure coefficients obtained at each orifice against  $x/c$ , fairing a smooth curve through the data points, and integrating this curve for area and moment about  $c/4$  simultaneously using a mechanical integrator. Figure 5 of reference 7 shows these faired curves used for the basic body configuration.

Total Wing Loads

The total normal force on the wing is

$$N_w = C_{N,w} q S = 2 \int_{\bar{x}}^{b/2} n \, dy$$

and

$$C_{N,w} = \frac{2}{qS} \int_{\bar{x}}^{b/2} c_n q c \, dy = \int_{\frac{\bar{x}}{b/2}}^1 c_n \frac{c}{c_{av}} d\left(\frac{y}{b/2}\right) \quad (3)$$

The bending moment about the wing-body center line is

$$M = C_{B,w} q \frac{S}{2} \frac{b}{2} = \int_{\bar{x}}^{b/2} c_n q c y \, dy$$

CONFIDENTIAL

and

$$C_{B,w} = \frac{2}{S} \frac{2}{b} \frac{1}{q} \int_{\bar{x}}^{b/2} c_n q c y \, dy = \int_{\frac{\bar{x}}{b/2}}^1 c_n \frac{c}{c_{av}} \left(\frac{y}{b/2}\right) d\left(\frac{y}{b/2}\right) \quad (4)$$

The integrals of equations (3) and (4) were evaluated simultaneously using a method similar to the one described for evaluating the integrals of equations (1) and (2).

In order to obtain the total wing pitching moment about a line passing through  $\bar{c}/4$ , the section pitching moment coefficients had to be transferred from  $c/4$  to  $\bar{c}/4$ . This was accomplished using the relation

$$c_m(\bar{c}/4) = c_m(c/4) + c_n \left( \frac{x_{\bar{c}/4}}{c} - \frac{x_{c/4}}{c} \right) \quad (5)$$

The wing pitching moment about  $\bar{c}/4$  is

$$M_v(\bar{c}/4) = C_m(\bar{c}/4) q S \bar{c} = 2 \int_{\bar{x}}^{b/2} c_m(\bar{c}/4) q c^2 dy$$

and

$$C_m(\bar{c}/4) = \int_{\frac{\bar{x}}{b/2}}^1 c_m(\bar{c}/4) \frac{c^2}{\bar{c} c_{av}} d \frac{y}{b/2} \quad (6)$$

The integral of equation (6) was evaluated using the same method used for equations (1) and (2).

CONFIDENTIAL

- 27 -

The wing spanwise, or lateral center of pressure location was obtained using the relation

$$\frac{y_{cp}}{b/2} = \frac{C_{B,w}}{C_{N,w}} \quad (7)$$

and the wing chordwise center of pressure obtained using the relation

$$\frac{x_{cp}}{\bar{c}} = 0.25 - \frac{C_m(\bar{c}/4)}{C_{N,w}} \quad (8)$$

Body Loads

The normal force coefficient for the body, based on wing area, is

$$C_{N,fw} = \frac{2\pi D_{max}}{S} \int_0^{1/4} \int_0^1 (C_{p,L} - C_{p,U}) \frac{r}{r_{max}} \cos \theta d\left(\frac{x}{l}\right) d\left(\frac{\theta}{2\pi}\right) \quad (9)$$

and the pitching-moment coefficient about  $\bar{c}/4$ , based on wing area and  $\bar{c}$ , is

$$C_{m,fw} = \frac{2\pi l^2 D_{max}}{S \bar{c}} \int_0^{1/4} \int_0^1 (C_{p,L} - C_{p,U}) \left( \frac{x\bar{c}/4 - x}{l} \right) \cos \theta \frac{r}{r_{max}} d\left(\frac{x}{l}\right) d\left(\frac{\theta}{2\pi}\right) \quad (10)$$

In order to evaluate the integrals in equations (9) and (10), the integrals were grouped as follows:

$$C_{N,fw} = \frac{2\pi l D_{max}}{S} \int_0^{1/4} \left\{ \int_0^1 (C_{p,L} - C_{p,U}) \frac{r}{r_{max}} d\left(\frac{x}{l}\right) \right\} \cos \theta d\left(\frac{\theta}{2\pi}\right) \quad (9a)$$

CONFIDENTIAL

$$C_{m, fw} = \frac{2\pi l^2 D_{\max}}{S \bar{c}} \int_0^{1/4} \left\{ \int_0^1 (C_{p, L} - C_{p, U}) \frac{r}{r_{\max}} \left( \frac{x \bar{c}/4 - x}{l} \right) d\left(\frac{x}{l}\right) \right\} \cos \theta d\left(\frac{\theta}{2\pi}\right) \quad (10a)$$

It is now apparent that the integration over  $x/l$  for (9a) and (10a) can be performed simultaneously using a technique similar to that used for equations (1) and (2). Then the integrations over  $(\theta/2\pi)$  were performed separately by multiplying the result from the first integration by  $\cos \theta$ , plotting versus  $(\theta/2\pi)$  and integrating mechanically.

#### Wing Body Loads

Loading parameters for the wing-body combination were obtained by algebraic addition of the parameters from the wing and body, that is

$$C_N = C_{N, w} + C_{N, fw} \quad (11)$$

$$C_m = C_{m, w} + C_{m, fw} \quad (12)$$

CONFIDENTIAL

- 29 -

IX. THEORETICAL CONSIDERATIONS

It would be very desirable to predict theoretically the aerodynamic loading characteristics for a given configuration. If the real configurations behave as do those of linear theory the loading due to camber will not change with angle of attack and can be added to the loading due to angle of attack alone to provide the total loading. The experimental data presented herein is available in a form which lends itself to a theoretical treatment, that is, the effects of camber and angle of attack can be isolated. The theoretical methods to determine the loading due to camber are long and cumbersome and will not be considered herein. However much useful information about the configuration can be obtained from the loading due to angle of attack alone. Reference 13 presents a method for determining the aerodynamic loading due to angle of attack on a slender wing-body combination. This reference shows that if the wing-body combination can be considered slender, that is, consists of a slender pointed body and a pointed low-aspect-ratio wing, then the Prandtl linearized differential equation for the perturbation velocity potential for an inviscid compressible fluid in three dimensions reduces to a two dimensional equation. A consequence of this is that the loading and aerodynamic properties of the configuration are independent of Mach number. A simplified theory of this nature is ideal in that the time required to obtain the aerodynamic loading characteristics of a given configuration is short. Since the wing-body combination of this paper is approaching a slender one, it is of interest to assess the

CONFIDENTIAL

CONFIDENTIAL

- 30 -

ability of this simplified theory to predict the loading due to angle of attack for this configuration. Therefore calculations have been made using reference 13 and compared with experiment. The results are presented in the next section.

CONFIDENTIAL

CONFIDENTIAL

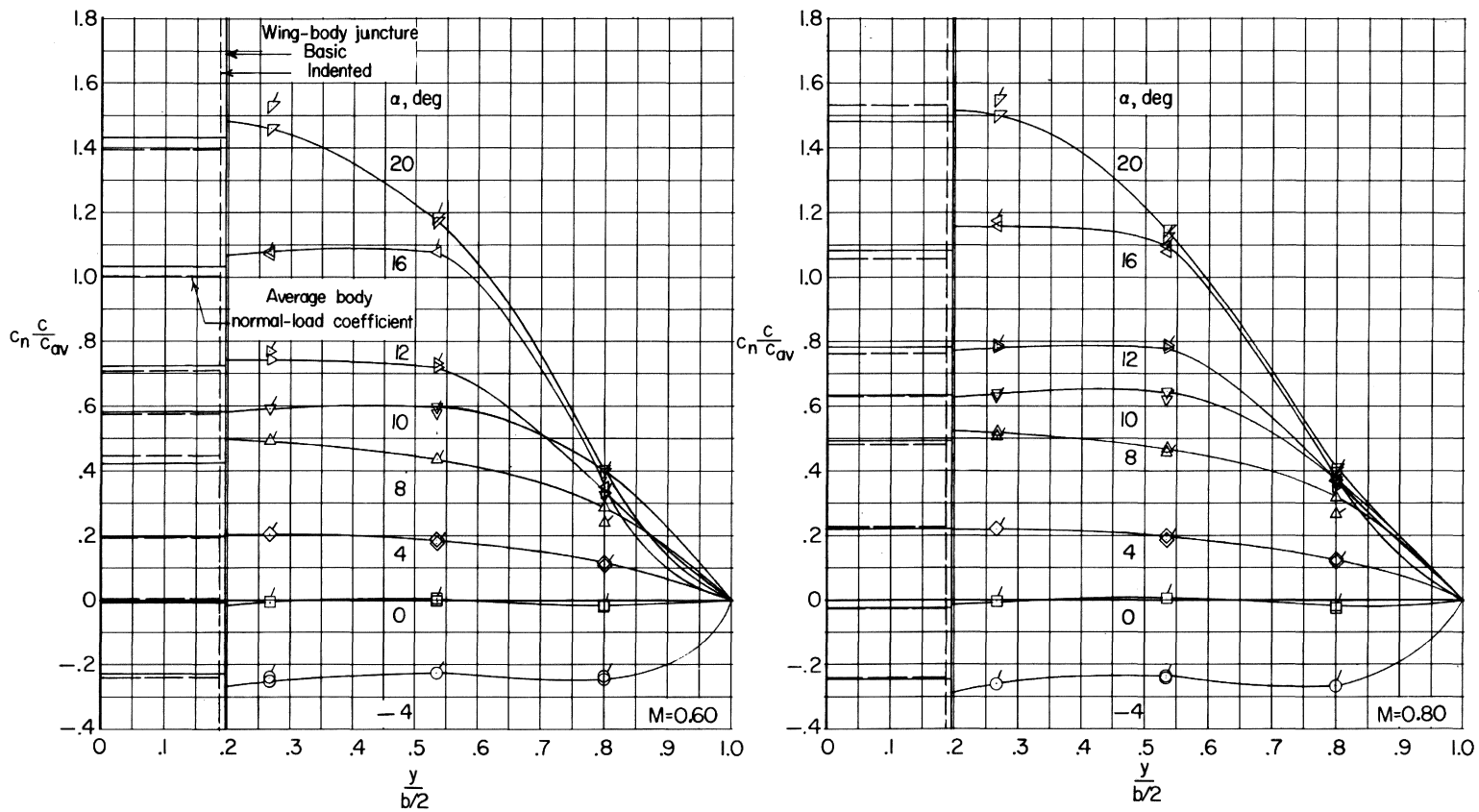
- 31 -

X. RESULTS AND DISCUSSION

Staggered scales have been used on many of the figures and care should be taken in selecting the proper reference axis for each curve. In Figure 3(d) note that data for the indented body configuration were not obtained at the two highest angles of attack. In Figures 6 and 7 note that force data for  $M = 1.43$  is not available for the configurations.

Spanwise load distributions.- At an angle of attack of  $0^\circ$  the spanwise load distributions (Fig. 3) generally showed a small negative loading over the majority of the span. This would be expected, however, since with this type of camber the outboard wing sections are operating at a lower angle of attack than the wing-body center line. As the angle of attack is increased to  $+4^\circ$  at  $M = 0.6$  (Fig. 3(a)) the spanwise load distribution becomes approximately elliptical in shape. Further increases in angle of attack cause the shape to deviate from elliptical and approach triangular at the highest angle tested. Examination of the chordwise pressure distributions in reference 7 has indicated the presence of a leading-edge separation vortex over the wing at moderate to high angles of attack. This vortex causes radical changes in the chordwise pressure distributions at the outboard stations (see Fig. 5(a), ref. 7) which result in the changes in shape noted for the spanwise load distributions. As the Mach number is increased above  $M = 1.0$ , the effect of this vortex on the spanwise load distributions is not as prominent as it was at the lower Mach numbers

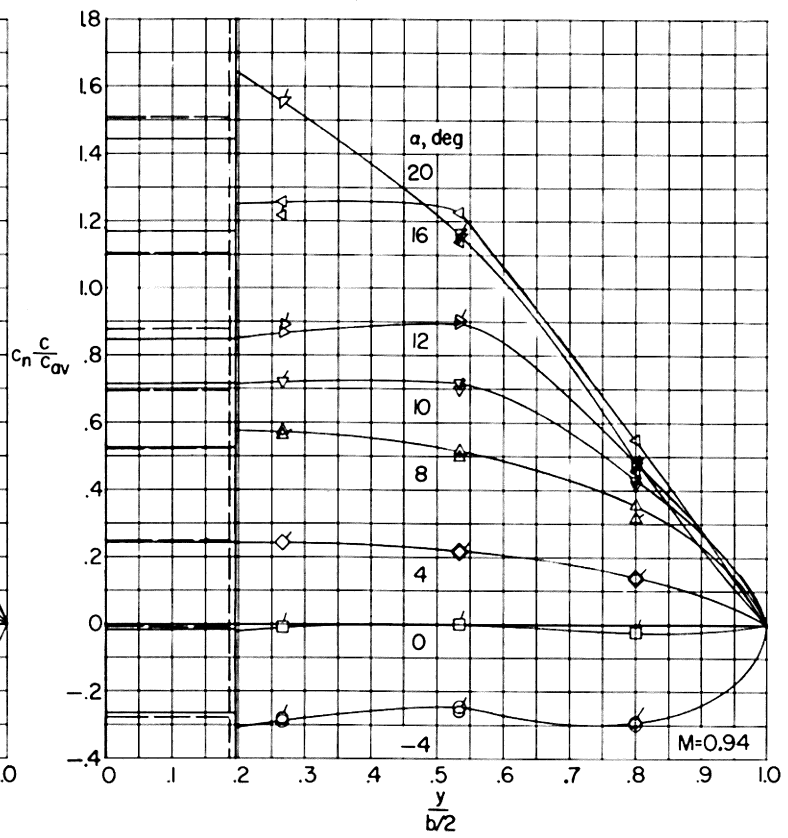
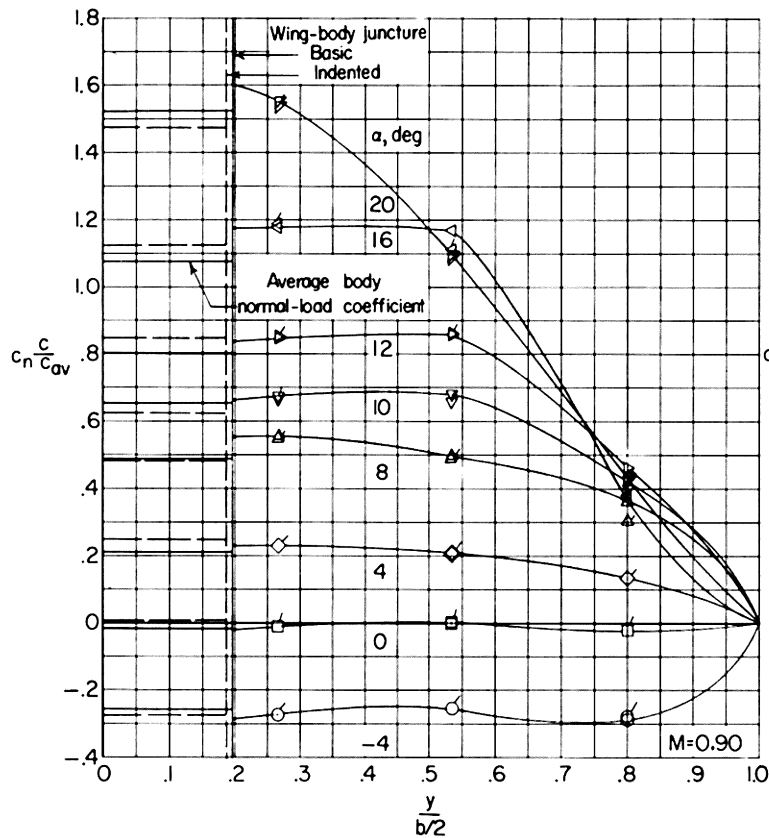
CONFIDENTIAL



(a)  $M = 0.60$  and  $0.80$ .

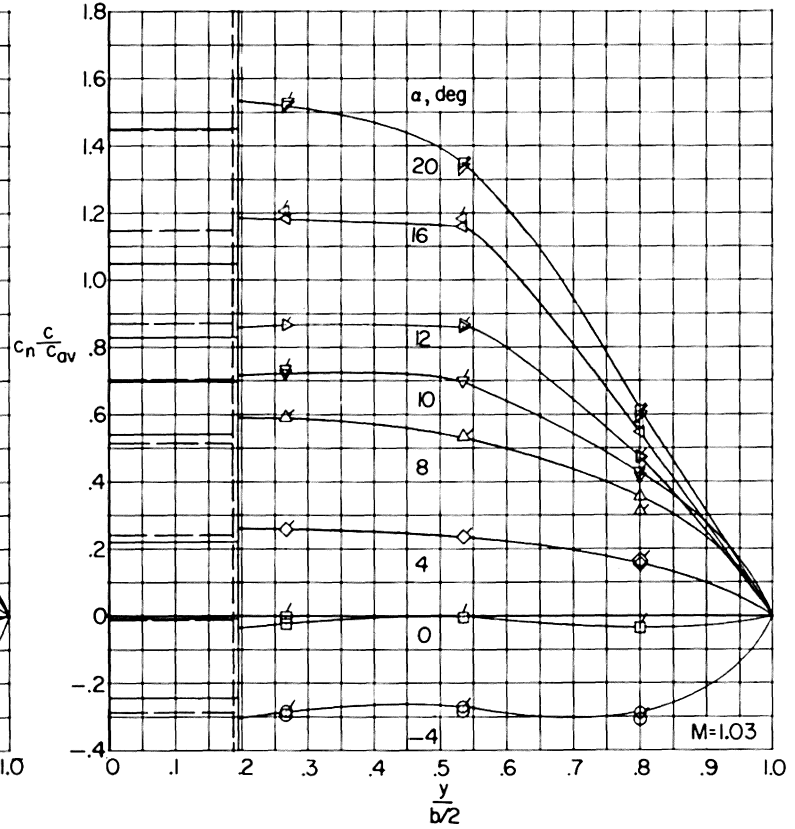
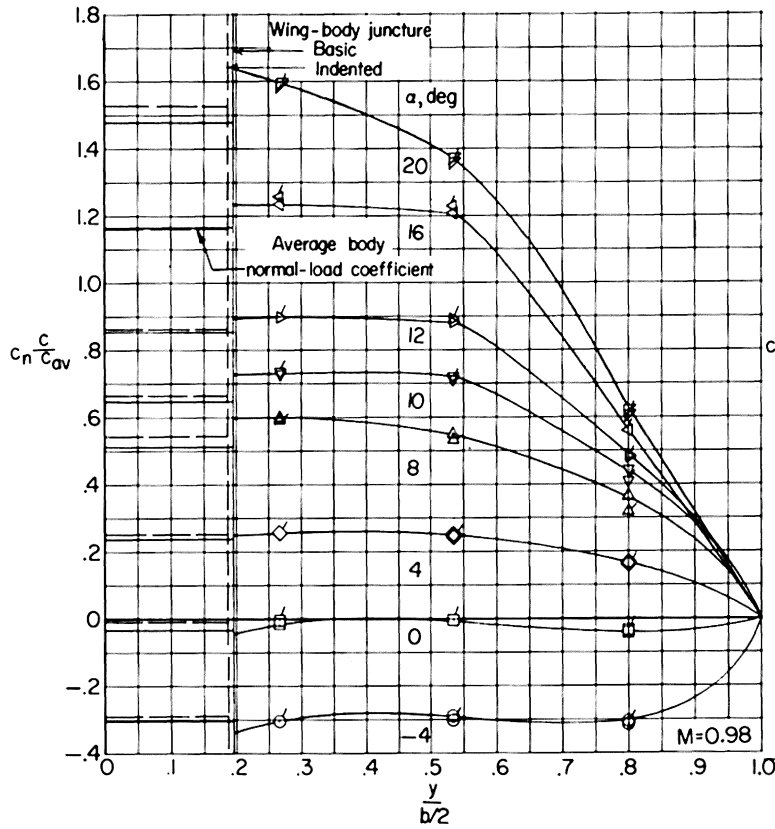
Figure 3.- Spanwise load distributions. Flagged symbols and dashed lines indicate indented body data.





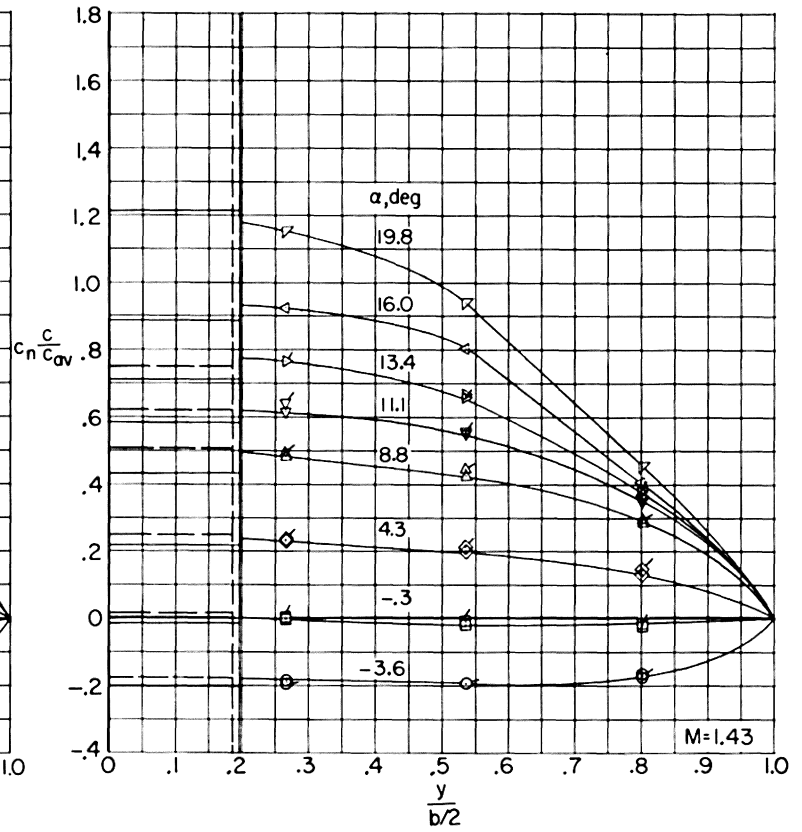
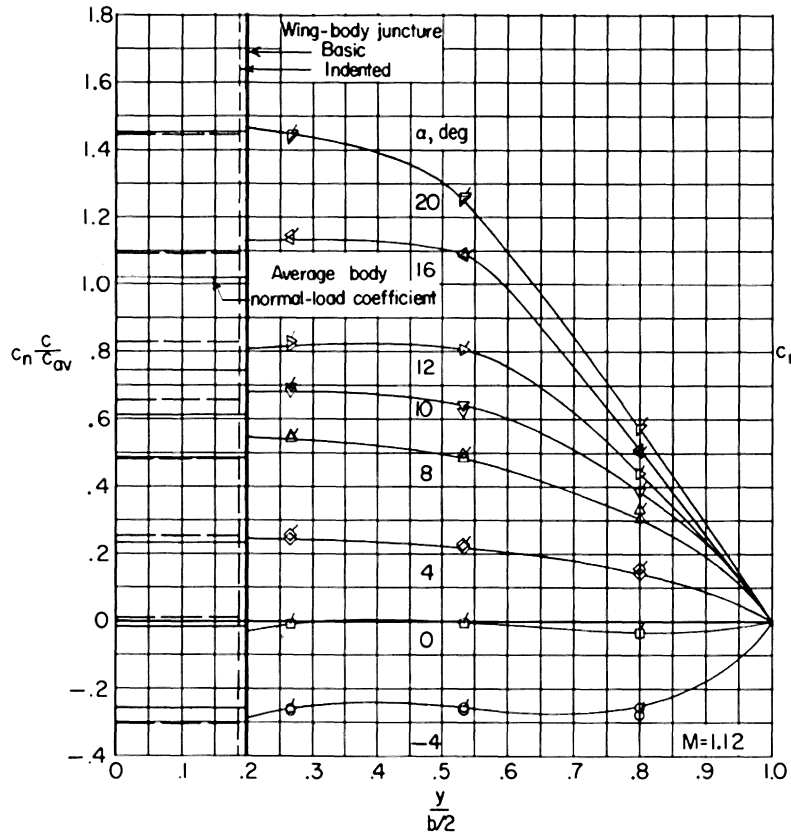
(b)  $M = 0.90$  and  $0.94$ .

Figure 3.- Continued.



(c)  $M = 0.98$  and  $1.03$ .

Figure 3.- Continued.



(d)  $M = 1.12$  and  $1.43$ .

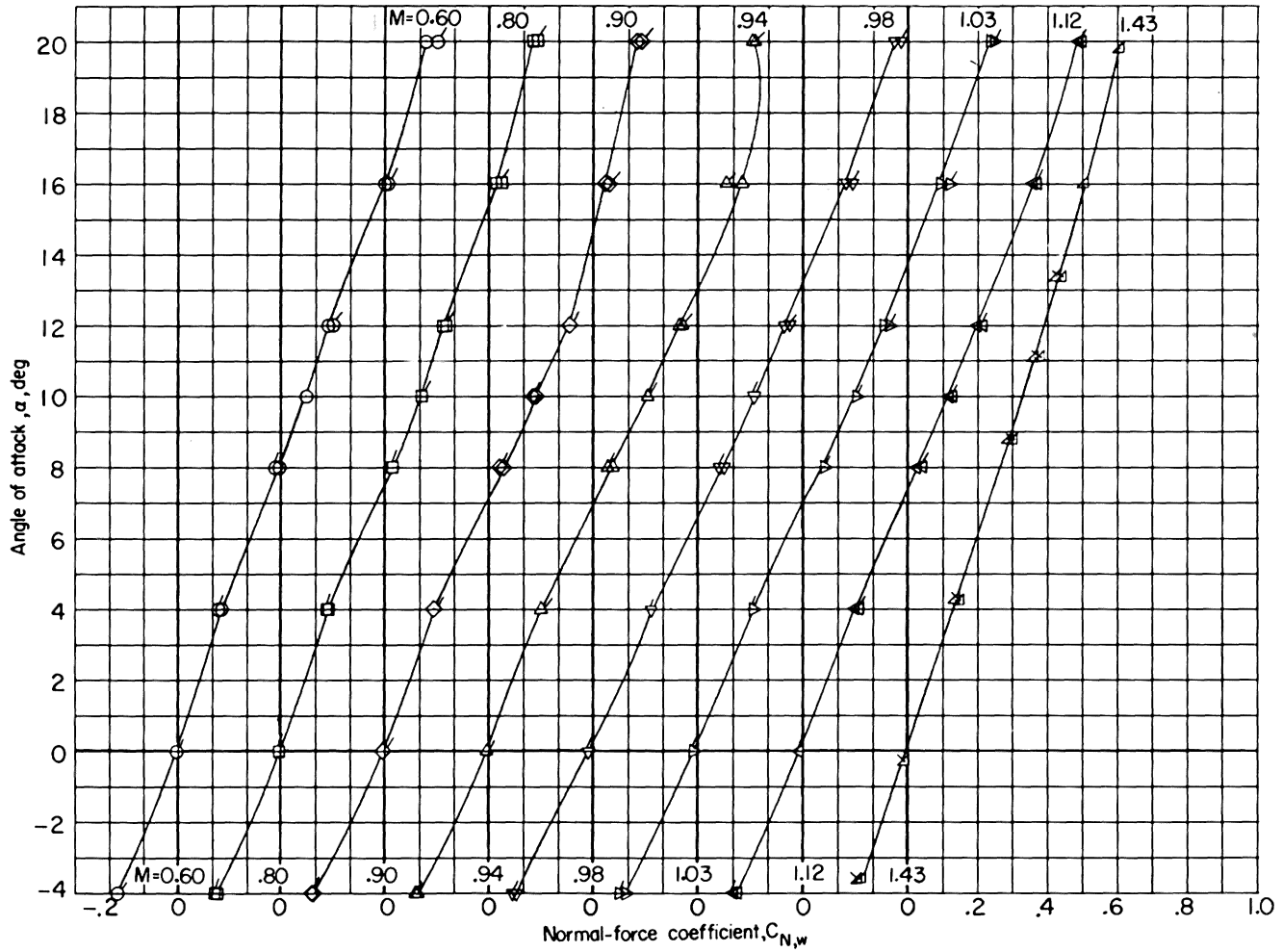
Figure 3.- Concluded.

(Figs. 3(b) through 3(d)). However there is indication that it is still present on the wing even at a Mach number of 1.43. At the negative angle of attack of  $-4^{\circ}$  the shape of the spanwise load distribution is somewhat unusual at all Mach numbers except 1.43. The chordwise pressure distributions of reference 7 indicated that the leading-edge separation vortex had already formed on the wing at this angle of attack.

The wing-body juncture locations for the basic and indented bodies shown on Figure 3 were obtained by taking the root-mean-square value of the body radius over the region of the body intersected by the wing. The resulting values were  $0.198b/2$  and  $0.188b/2$  for the basic and indented bodies, respectively.

Also shown on Figure 3 is the average body normal-load coefficient for both the basic and indented configurations. This coefficient is defined so the area under this curve from the wing-body center line to the wing-body juncture is equal to the normal force coefficient for the body in the presence of the wing. Therefore it indicates the average magnitude rather than the distribution of the load over the body.

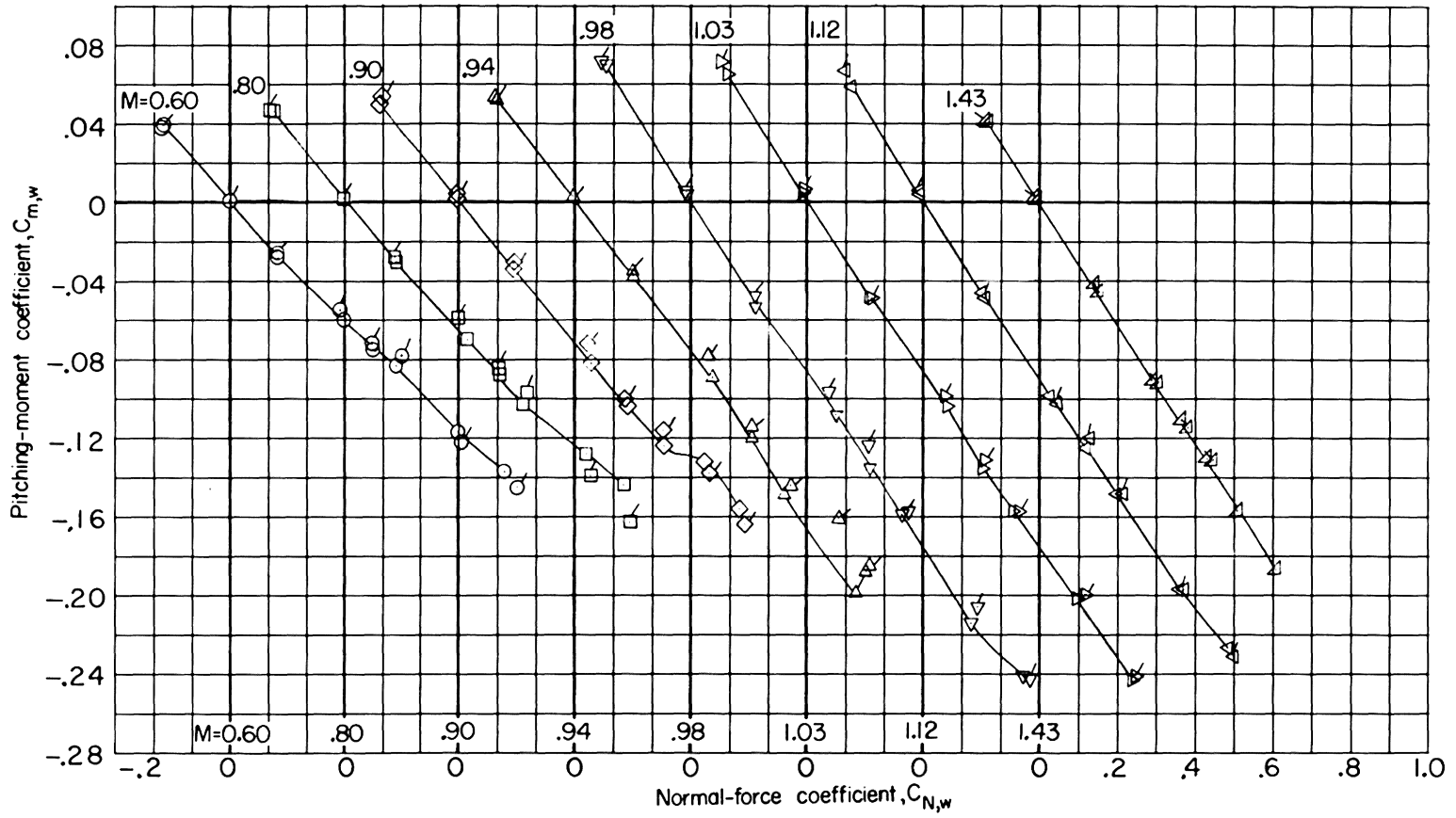
Force and moment characteristics.- The aerodynamic force and moment characteristics for the wing in the presence of the body (Fig. 4) and for the body in the presence of the wing (Fig. 5) were combined to obtain the aerodynamic characteristics for the wing-body combination (Figs. 6 and 7). The data of Figures 6 and 7 shows that, in general, both the force and moment coefficient curves exhibited nonlinearities even at low normal-force coefficients. This is a result of the



(a)  $\alpha$  versus  $C_{N,w}$ .

Figure 4.- Aerodynamic characteristics of the wing in the presence of the body. Flagged symbols denote data for the indented body.

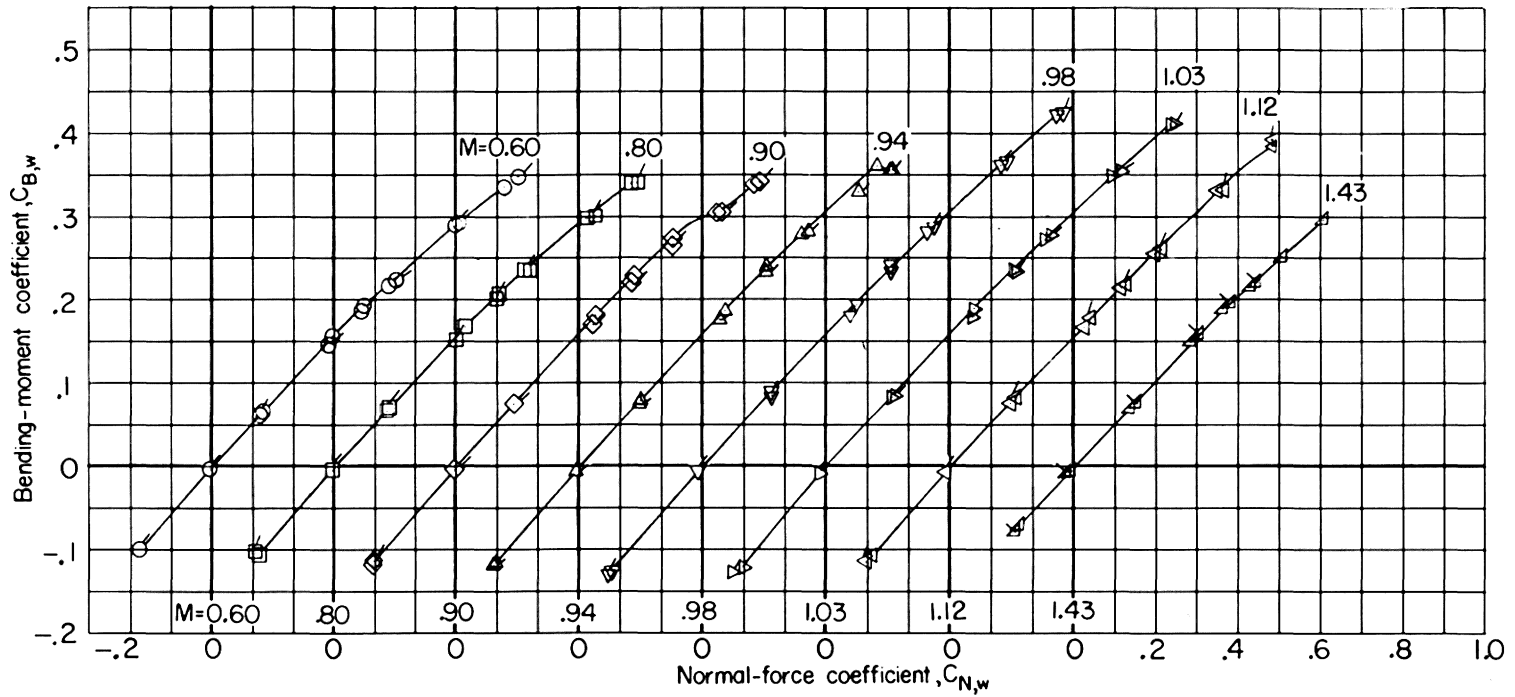
CONFIDENTIAL



(b)  $C_{m,w}$  versus  $C_{N,w}$ .

Figure 4.- Continued.

CONFIDENTIAL



(c)  $C_{B,w}$  versus  $C_{N,w}$ .

Figure 4.- Concluded.

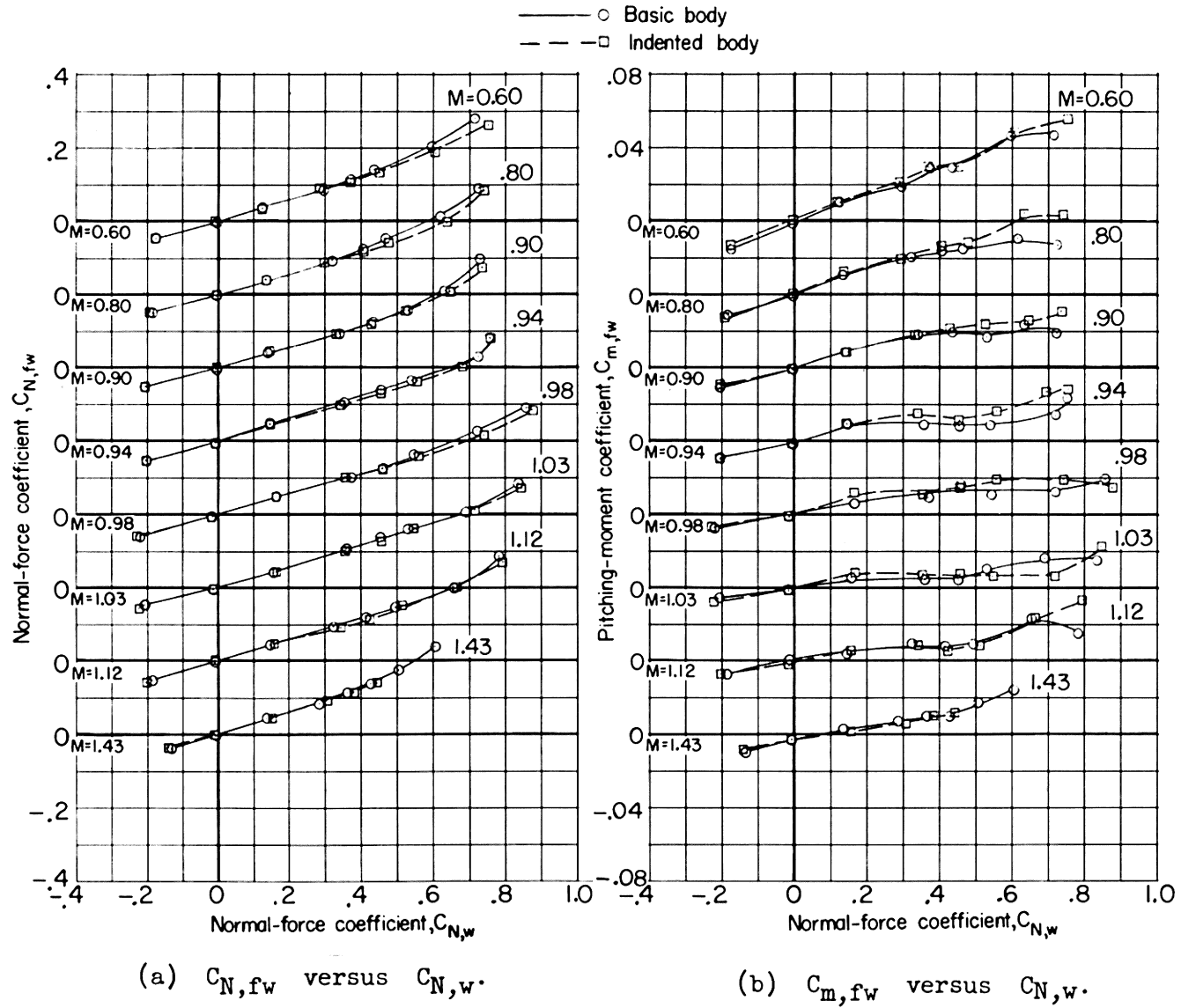
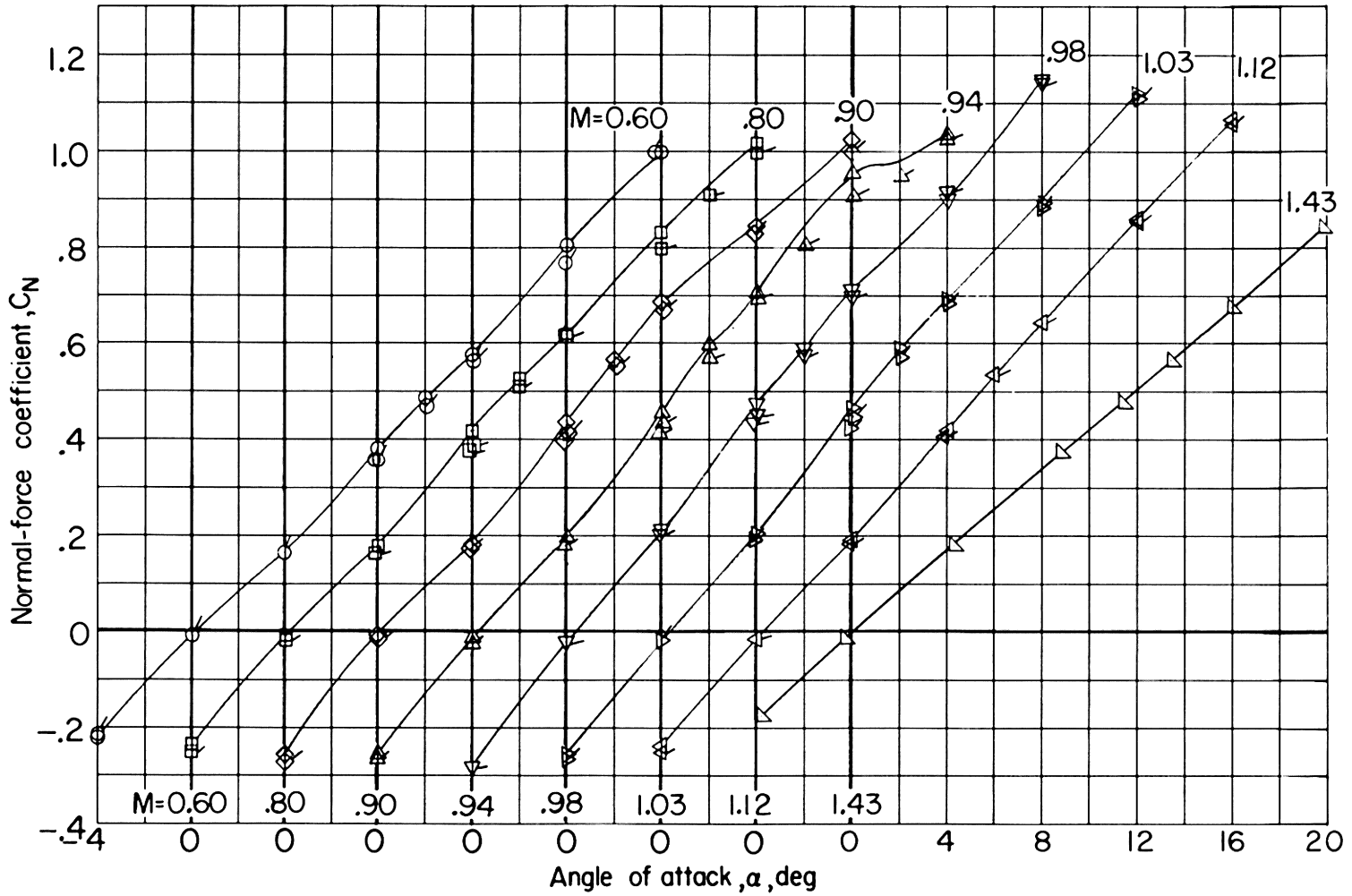


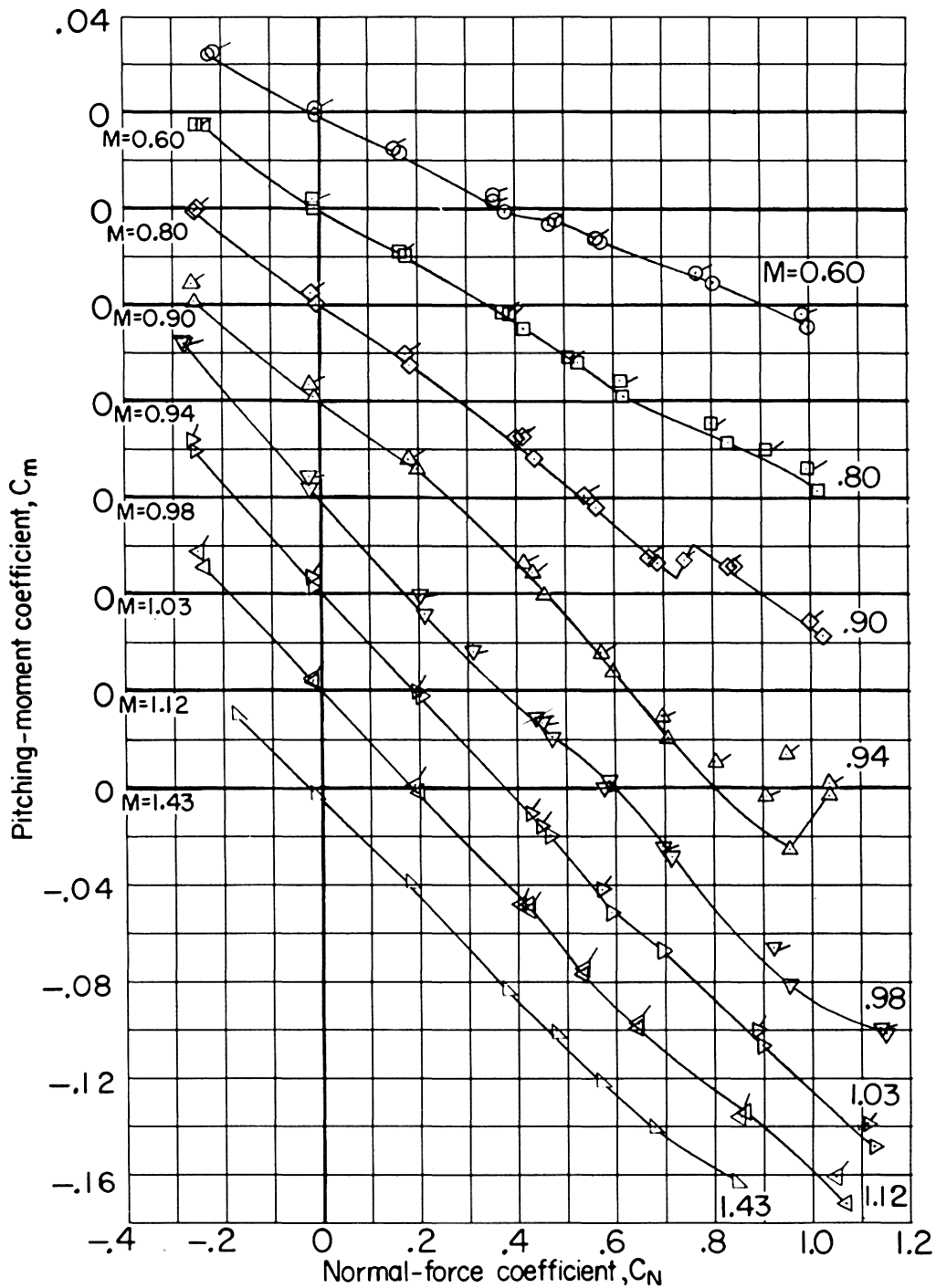
Figure 5.- Aerodynamic characteristics of the basic and indented bodies in the presence of the wing.





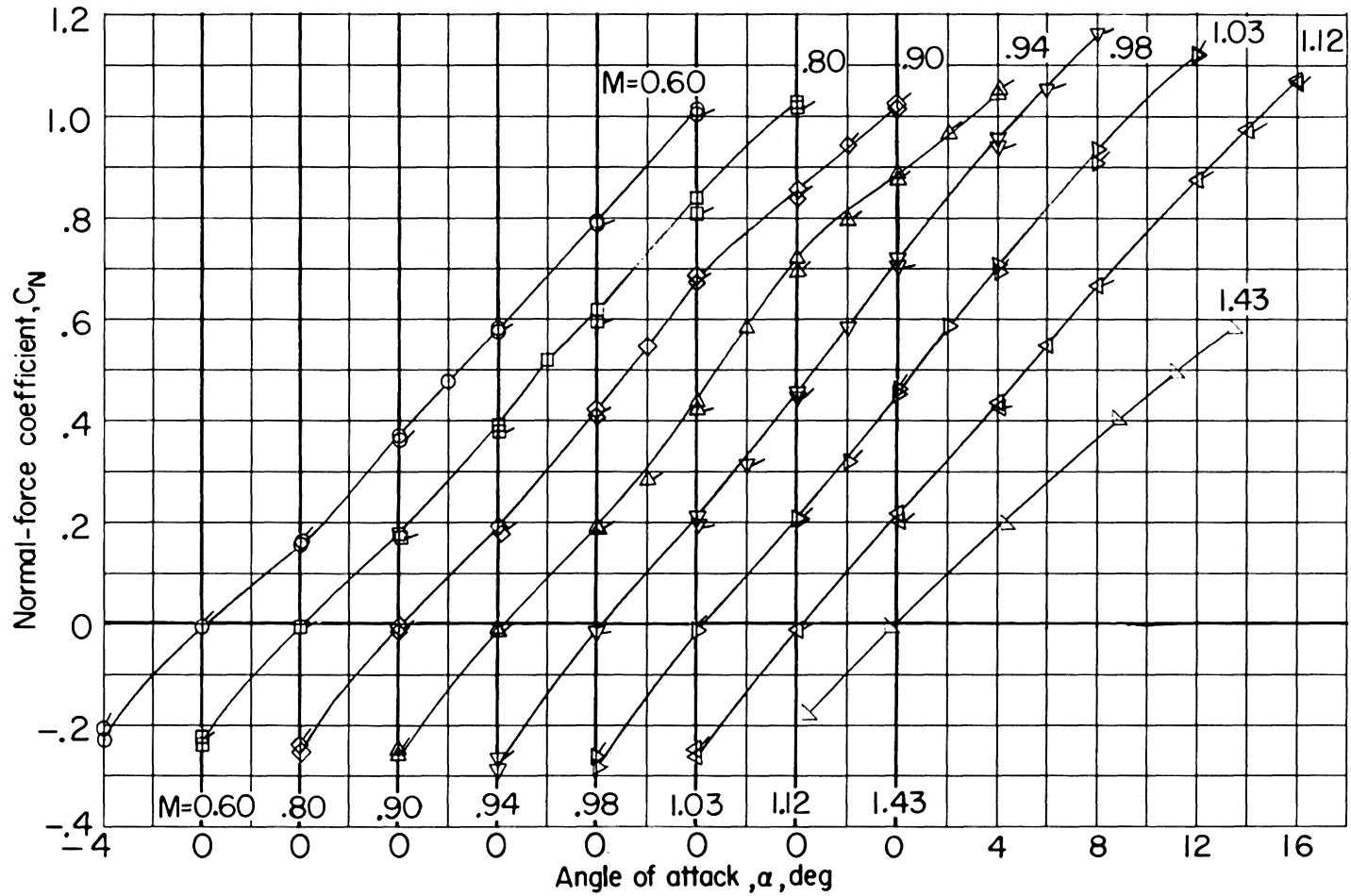
(a)  $C_N$  versus  $\alpha$ .

Figure 6.- Aerodynamic characteristics of the basic wing-body combination. Flagged symbols denote force data for same configuration from reference 2.



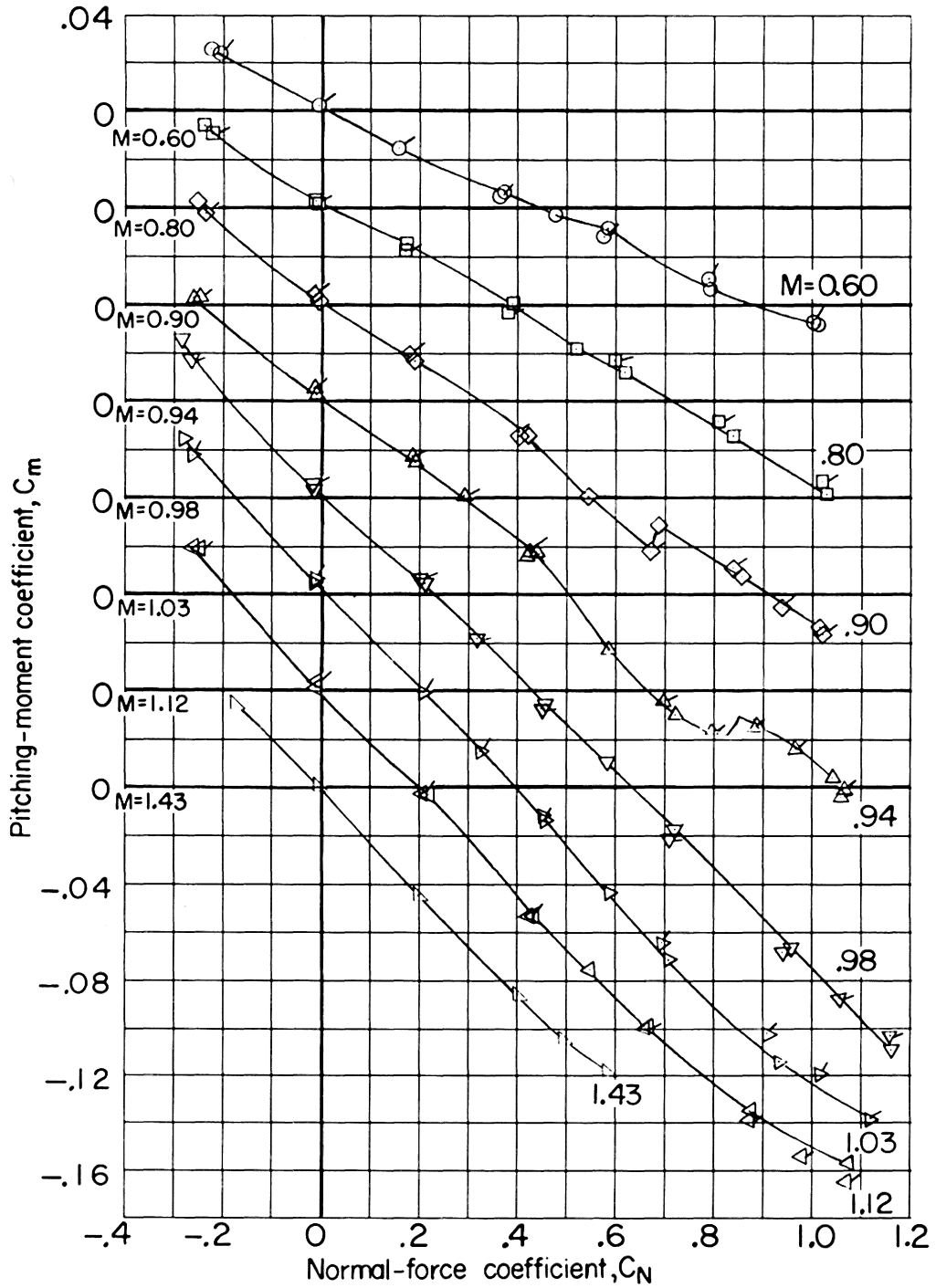
(b)  $C_m$  versus  $C_N$ .

Figure 6.- Concluded.



(a)  $C_N$  versus  $\alpha$ .

Figure 7.- Aerodynamic characteristics of the indented wing-body combination. Flagged symbols denote force data for same configuration from reference 2.



(b)  $C_m$  versus  $C_N$ .

Figure 7.- Concluded.

CONFIDENTIAL

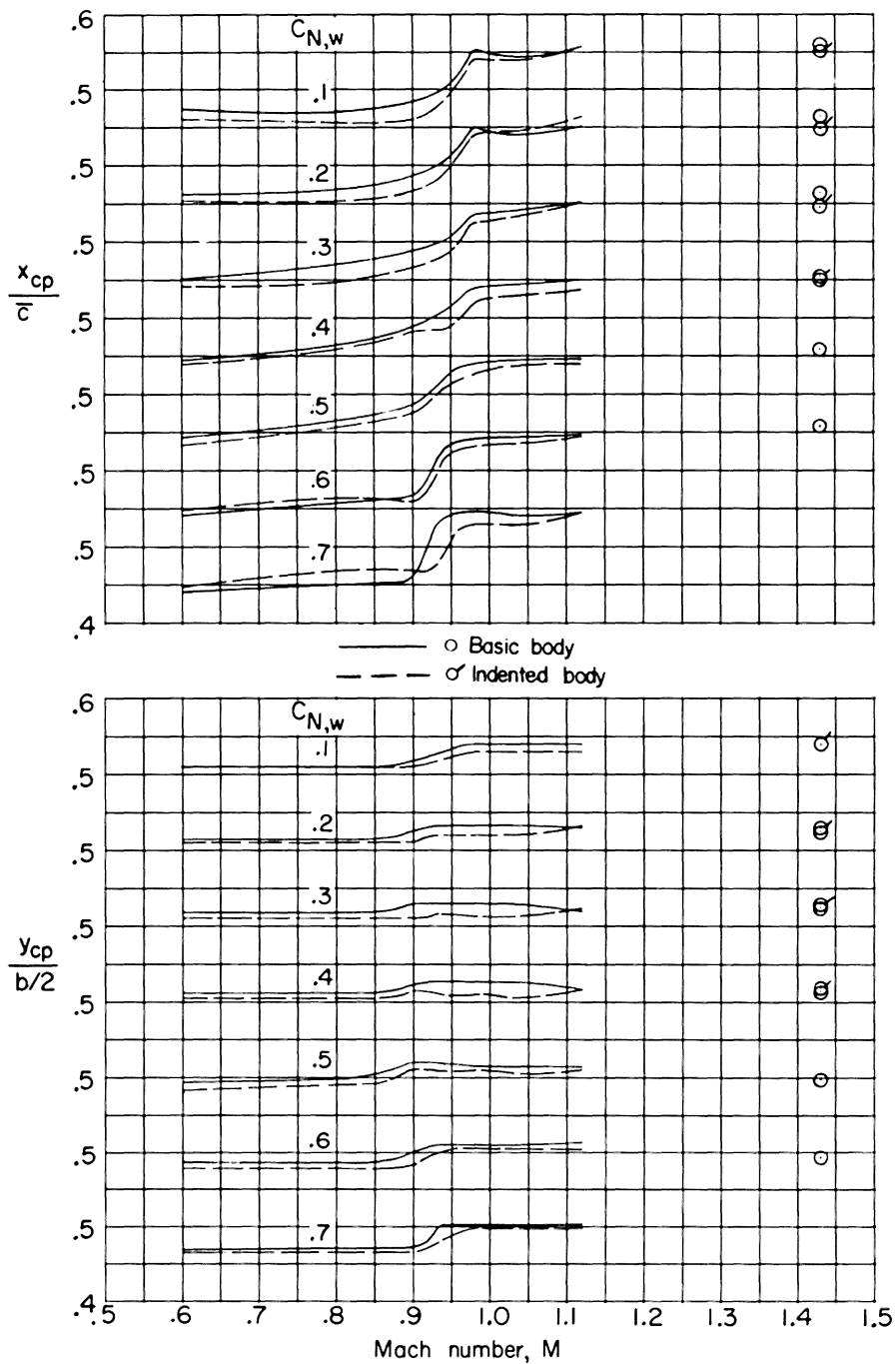
- 45 -

formation of the leading-edge separation vortex on the wing at low angles of attack as noted previously. At the higher normal-force coefficients an abrupt destabilizing tendency (Figs. 6(b) and 7(b)), which is characteristic of sweptback wings, is apparent at subsonic speeds.

Also shown on Figures 6 and 7 is a comparison between the force and moment characteristics obtained by integrating the pressure distributions and those obtained on the same configuration from the force tests of reference 2. The agreement between these two sets of data is very encouraging, particularly when it is considered that the pressure wing had chordwise rows of orifices at only three spanwise positions.

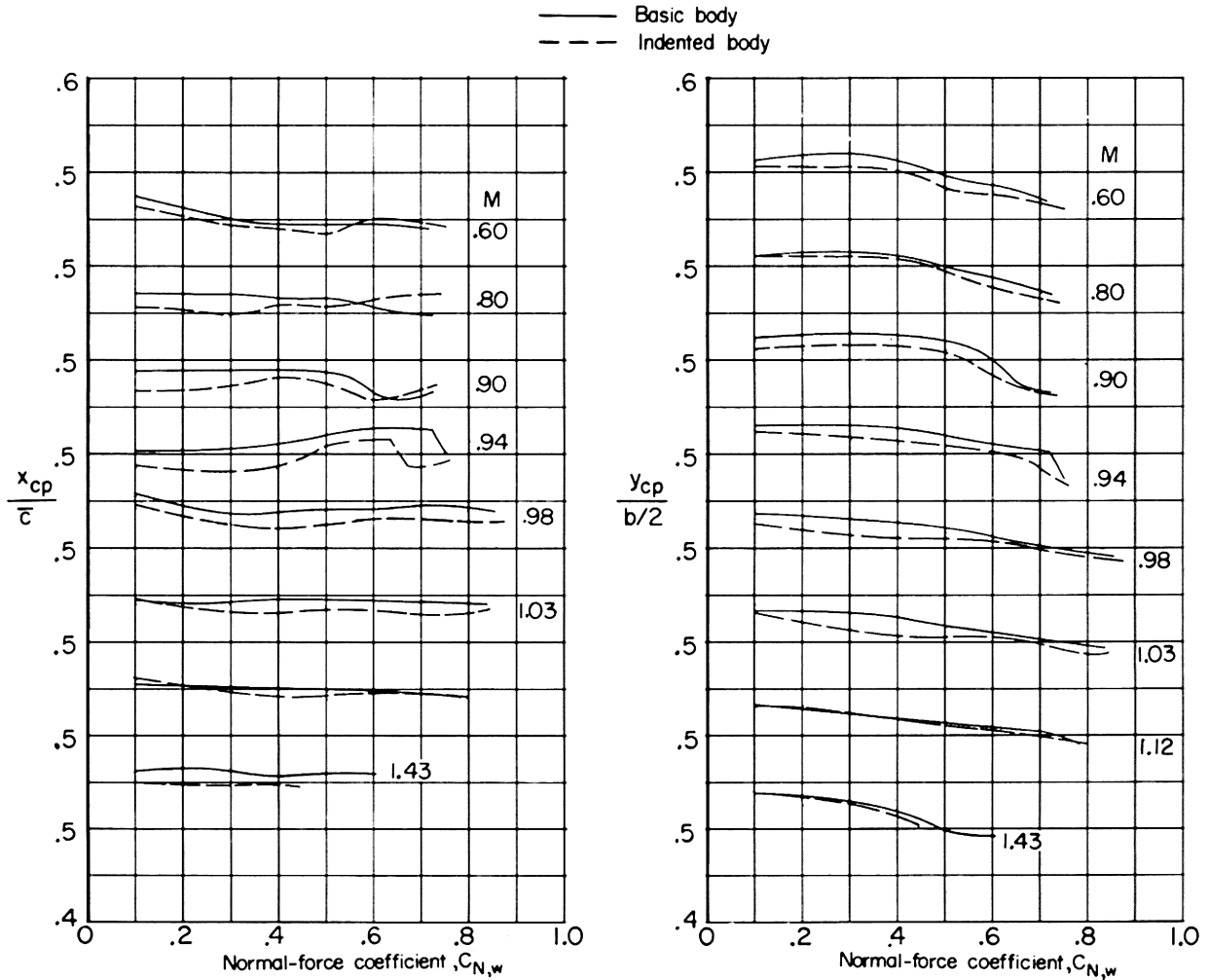
Center of pressure characteristics.- Significant center of pressure movements were noted in the transonic speed range through the range of normal force coefficients tested (Fig. 8(a)). Between  $M = 0.85$  and  $M = 1.0$  the center of pressure moved rearward and outboard rather abruptly. As the Mach number was increased further at a constant normal force coefficient, the center of pressure location appeared to begin to stabilize at its supersonic value. The effect of the abrupt destabilizing tendency, noted in Figures 6(b) and 7(b), on the center of pressure locations can be seen in Figure 8(b). Significant forward and inboard movements are apparent through a Mach number of 0.94. Of course the magnitude and abruptness of these

CONFIDENTIAL



(a) Variation with Mach number.

Figure 8.- Variation of longitudinal and lateral location of center of pressure.



(b) Variation with wing normal-force coefficient.

Figure 8.- Concluded.

CONFIDENTIAL

- 48 -

movements are consistent with the moment curves of Figures 4(c), 6(b), and 7(b).

Division of normal load.- Figure 9 shows that at low normal force coefficients the division of normal load was little affected by Mach number, the ratio being about 0.77 or 0.78 through the Mach number range. Increases in normal force coefficient resulted in a decrease in the fraction of the load carried by the wing at all Mach numbers. The ratio of exposed wing area to total wing area, denoted for the two configurations by the lines labeled  $S_e/S$  on Figure 9, has been used in the past as a "rule of thumb" so to speak to indicate the fraction of total normal load carried by the wing. For this configuration this ratio gives a poor estimate of the experimental results.

Effects of body indentation.- Data for the indented body configuration is presented and compared with data for the basic body configuration on Figures 3, 4, 5, 8, and 9. Generally the effects of body indentation are small. Figure 8, which shows a comparison of the center of pressure characteristics for the basic and indented body configurations, indicates that body indentation caused a slight delay in the transonic rearward and outboard center of pressure movement (Fig. 8(a)). In addition, body indentation was responsible for some changes in center of pressure location at high normal force coefficients, particularly at  $M = 0.94$ .

Comparison with plane wing.- Pressure measurements on a plane delta wing of the same planform and airfoil sections as the wing discussed

CONFIDENTIAL



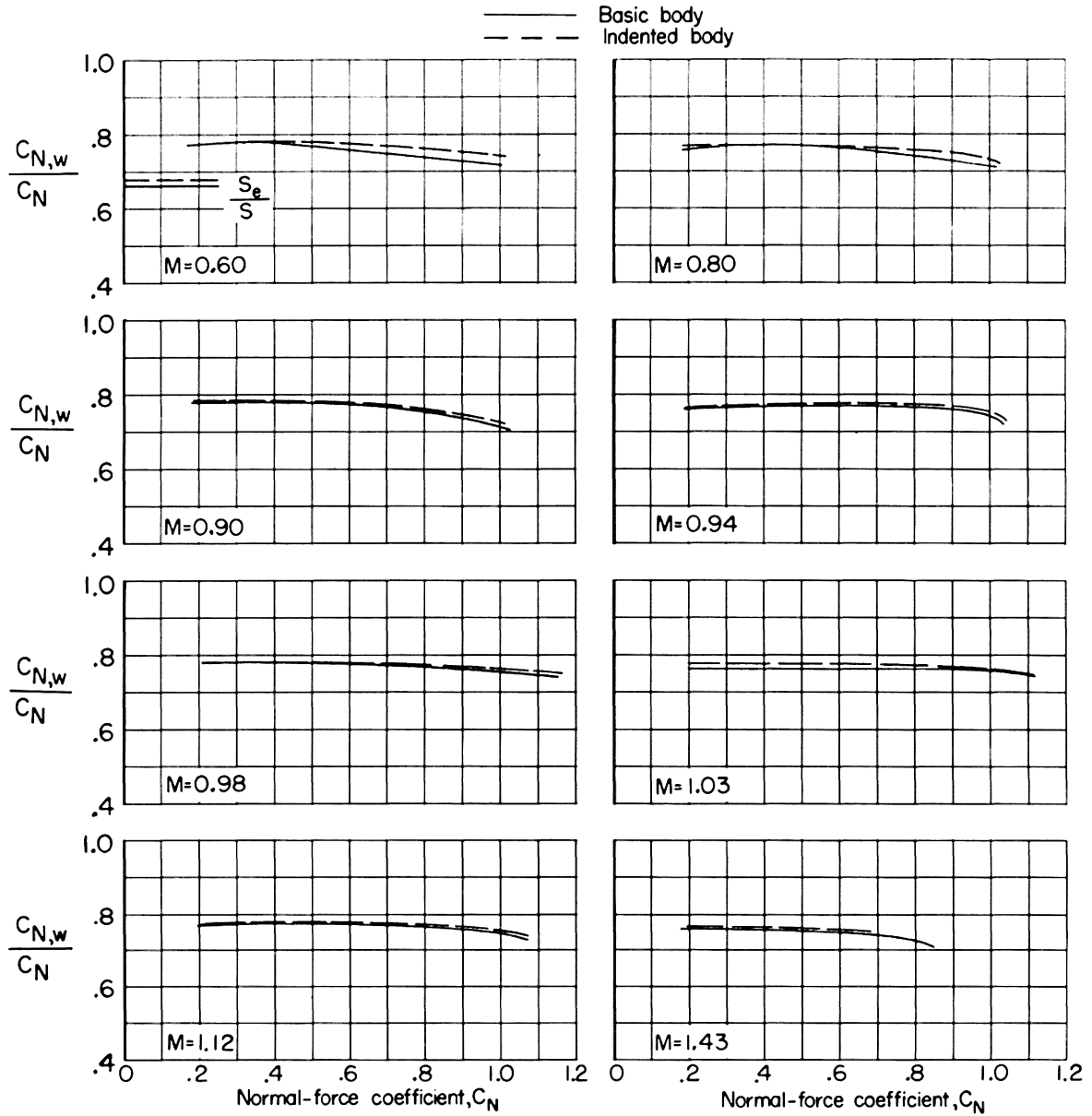


Figure 9.- Division of normal load.

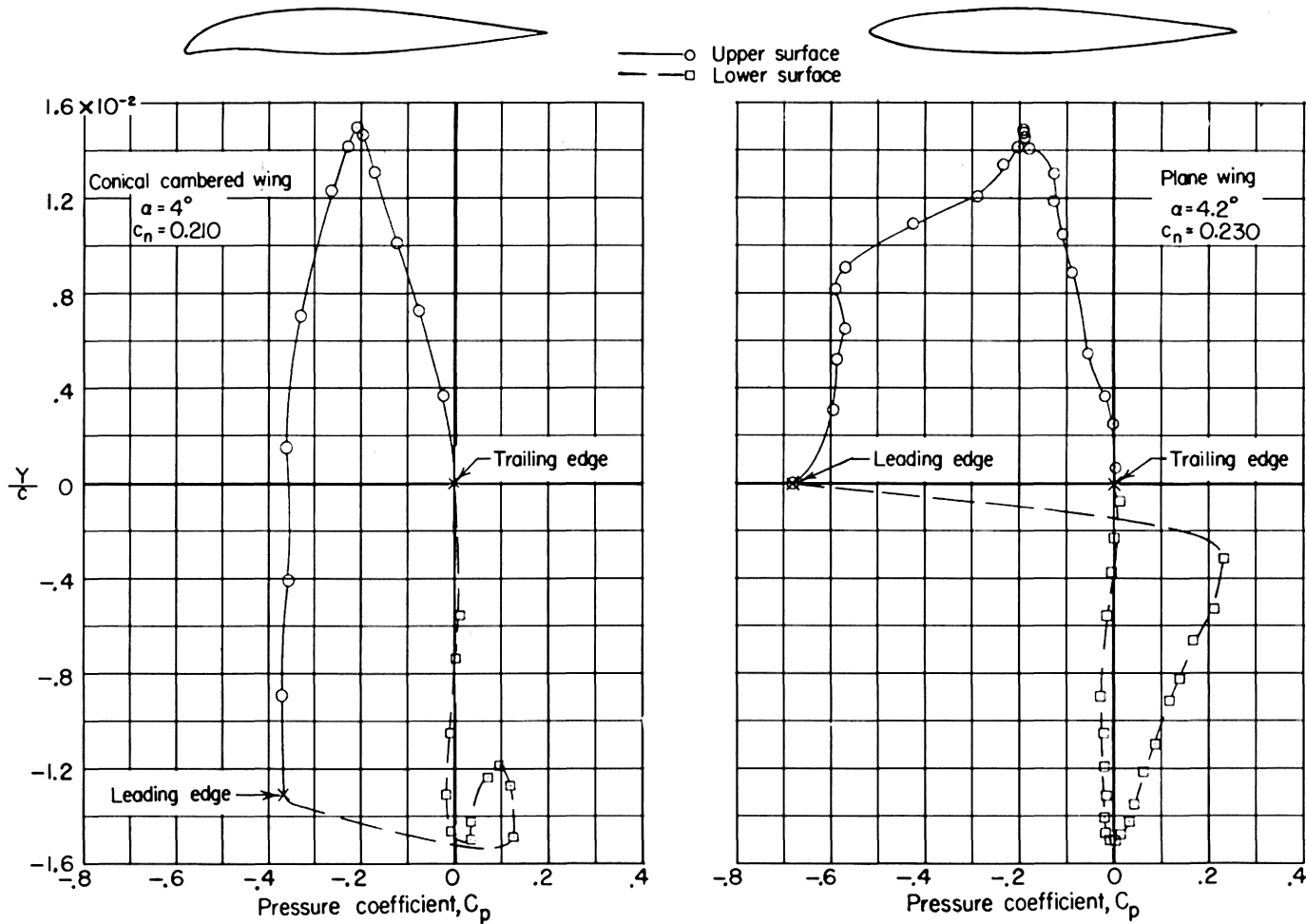
CONFIDENTIAL

- 50 -

herein are presented in reference 14. The body used in reference 14 is not identical to the body used for the present investigation, however the differences are small and will not invalidate the comparisons made herein.

As noted in the Introduction, a considerable performance benefit was realized when the plane wing was conically cambered. It is of interest to examine the mechanism that brings about this increase in performance. Reference 2 shows that at  $M = 0.8$  the maximum lift-drag ratio for the cambered wing is increased about 22 percent over the plane wing and this occurs at a lift coefficient of about 0.2. Therefore a comparison has been made at  $M = 0.8$  and  $\alpha \approx 4^\circ$  ( $C_L \approx 0.2$ ) of the pressure distributions at about midspan ( $\frac{y}{b/2} = 0.53$ ) on the plane and cambered wings to get an idea of a typical effect of camber. Figure 10(a) shows the pressure coefficient plotted against thickness in fraction of chord for the plane and cambered wings. The area enclosed is directly proportional to the amount of thrust or drag developed by the section, depending on whether the area is negative or positive. In traversing the curve starting at the leading edge, moving along the upper surface to the trailing edge and returning along the lower surface to the leading edge, area enclosed on your right results in negative drag or thrust. Likewise area enclosed to your left results in drag. It is evident from Figure 10(a) that the cambered wing develops all thrust whereas the plane wing has some drag associated with the

CONFIDENTIAL



(a)  $M = 0.80$ .

Figure 10.- Comparison of pressure distributions for the plane and cambered wings. Data for plane wing from reference 14.

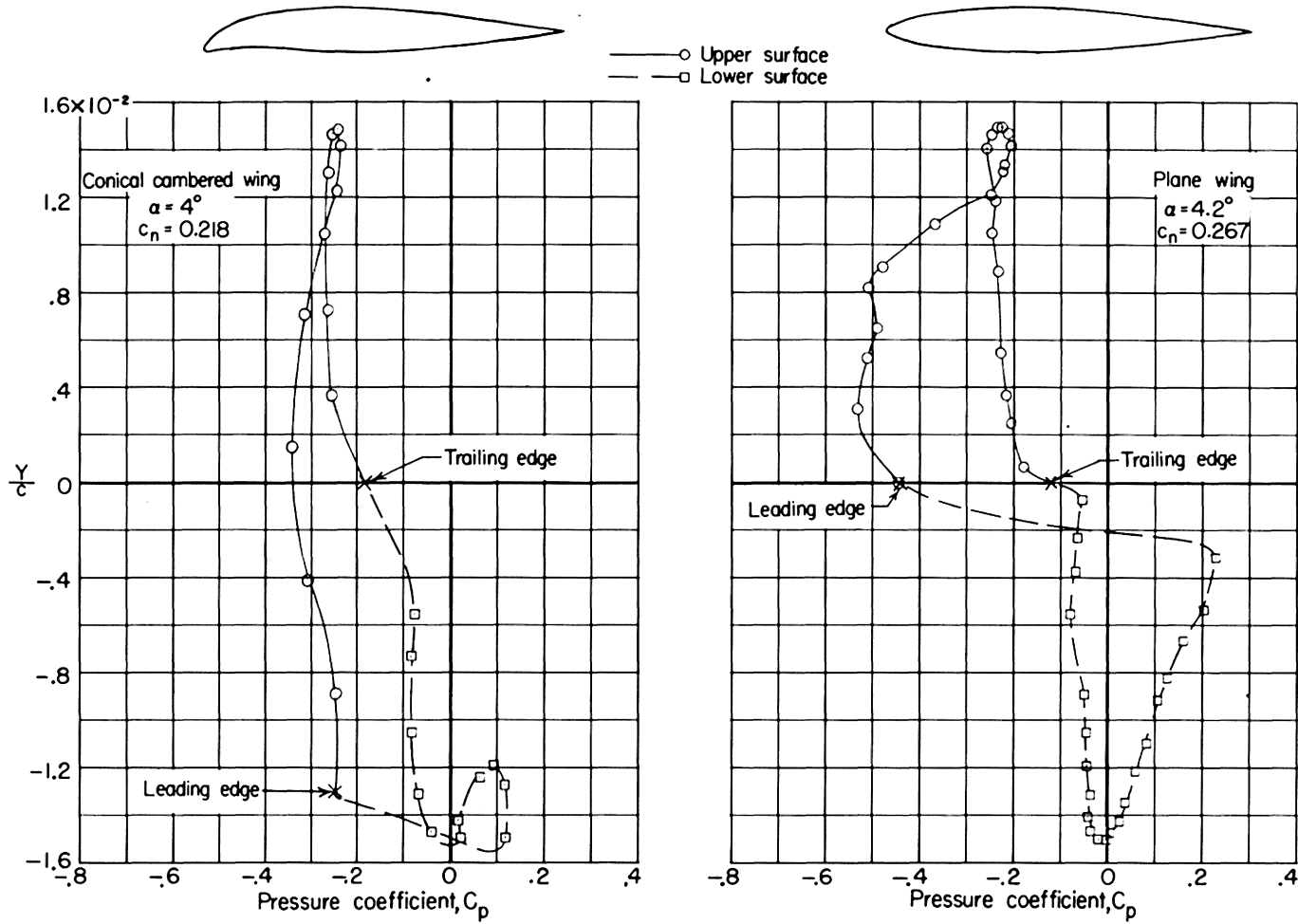
CONFIDENTIAL

- 52 -

pressures on the lower surface near the leading edge. The thrust developed by the cambered wing is about 1.8 times as large as the thrust developed by the plane wing. The result of this is that this section of the cambered wing developed about 61 percent of full leading edge suction whereas the plane wing developed only about 29 percent. These findings are consistent with the results noted from reference 2. Figure 10(b) shows the comparison at  $M = 1.03$ . It is readily apparent that increasing the Mach number from 0.80 to 1.03 was detrimental from a leading-edge thrust standpoint. The thrust produced by the cambered wing is still larger than that produced by the plane wing, however the magnitude has been reduced considerably. In this case the cambered wing developed about 23 percent of full leading-edge suction compared to about 5 percent for the plane wing. Again these results are consistent with force test results since reference 2 shows that the benefits due to camber diminish rapidly with increases in Mach number from 0.80 to 1.03.

It is of interest to note that although the peak negative pressures near the leading edge on the upper surface were considerably greater for the plane wing, the cambered wing developed more leading-edge thrust. The lesser pressures on the cambered wing acted over a much larger frontal area and the resultant force developed was greater. Also on the cambered wing the positive pressures on the lower surface near the leading edge produced thrust since this portion of the lower surface was properly inclined to the stream. It was noted previous that in this region on the plane wing a decrease in thrust resulted.

CONFIDENTIAL



(b)  $M = 1.03$ .

Figure 10.- Concluded.

CONFIDENTIAL

- 54 -

A decrement in the outboard loadings on the cambered wing would be expected when comparing to the plane wing since the camber resulted in the outer portions operating at a lower angle of attack than the wing-body center line. Figure 11, which presents a comparison of the spanwise load distributions for the plane and cambered wings, bears this out at about  $4^\circ$  angle of attack. However with increases in angle to about  $8^\circ$  the span load distribution for the plane wing deviated markedly from the approximately elliptical shape it had at  $4^\circ$  whereas the span load distribution for the cambered wing maintained the approximately elliptical shape (see Fig. 11(a)). Examination of the chordwise pressure distributions of references 7 and 14 indicate that the camber delayed the separation over the outboard sections of the wing to a higher angle of attack. This, in turn, is responsible for the differences in the shapes of the span loading at  $\alpha = 8^\circ$ . This outboard separation was not as pronounced at  $M = 1.03$  and  $\alpha = 4^\circ$  (Fig. 11(b)). At an angle of attack of about  $12^\circ$  both the plane and cambered wings appeared to be separated over the outboard region. However at  $M = 0.80$  the loading for the plane wing on the outboard sections is still below that for the cambered wing. At  $M = 1.03$  there are little differences in the span loading characteristics.

Comparison with theory.- Figure 12 presents a comparison between the experimental and theoretical loadings due to  $4^\circ$  angle of attack. The theoretical loading was computed using the method of reference 13 for the wing in combination with an infinite cylinder. The experimental

CONFIDENTIAL

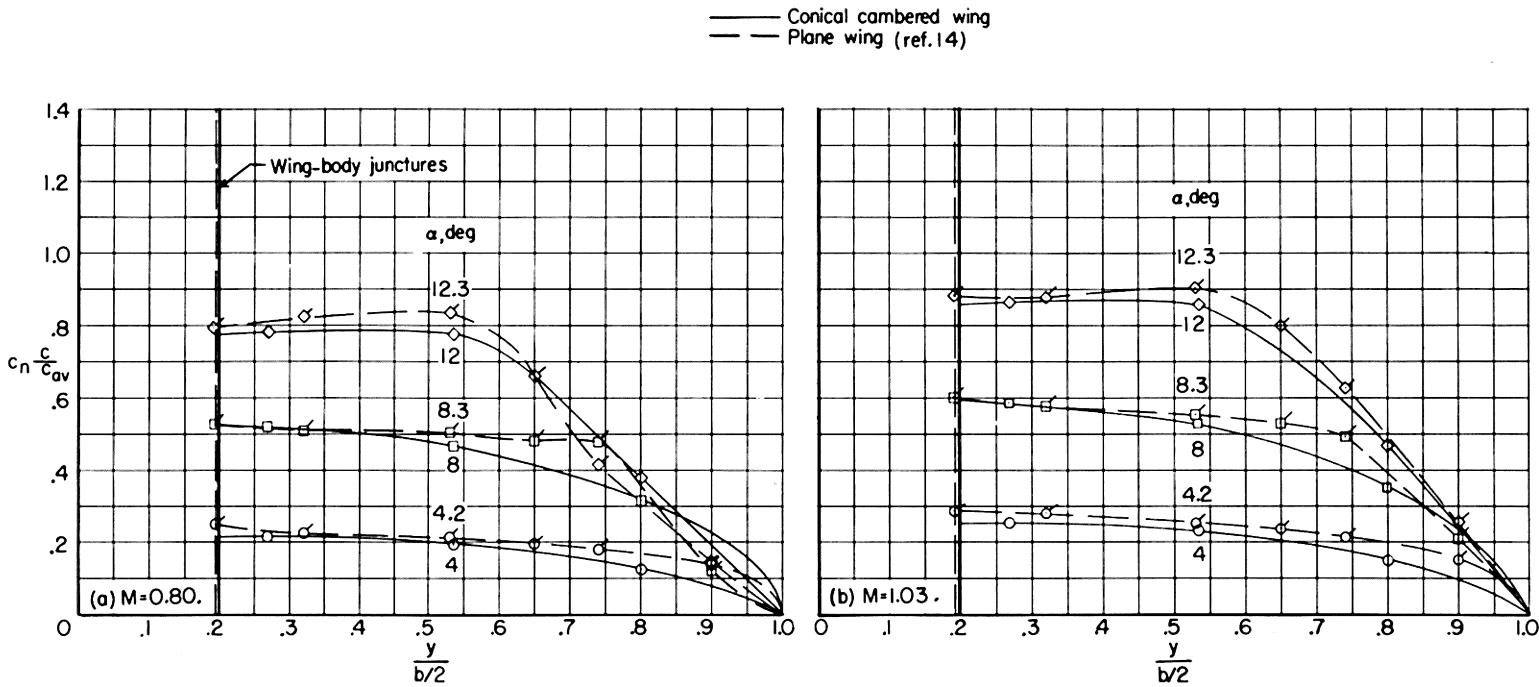


Figure 11.- Comparison of span loading characteristics for the plane and cambered wings.

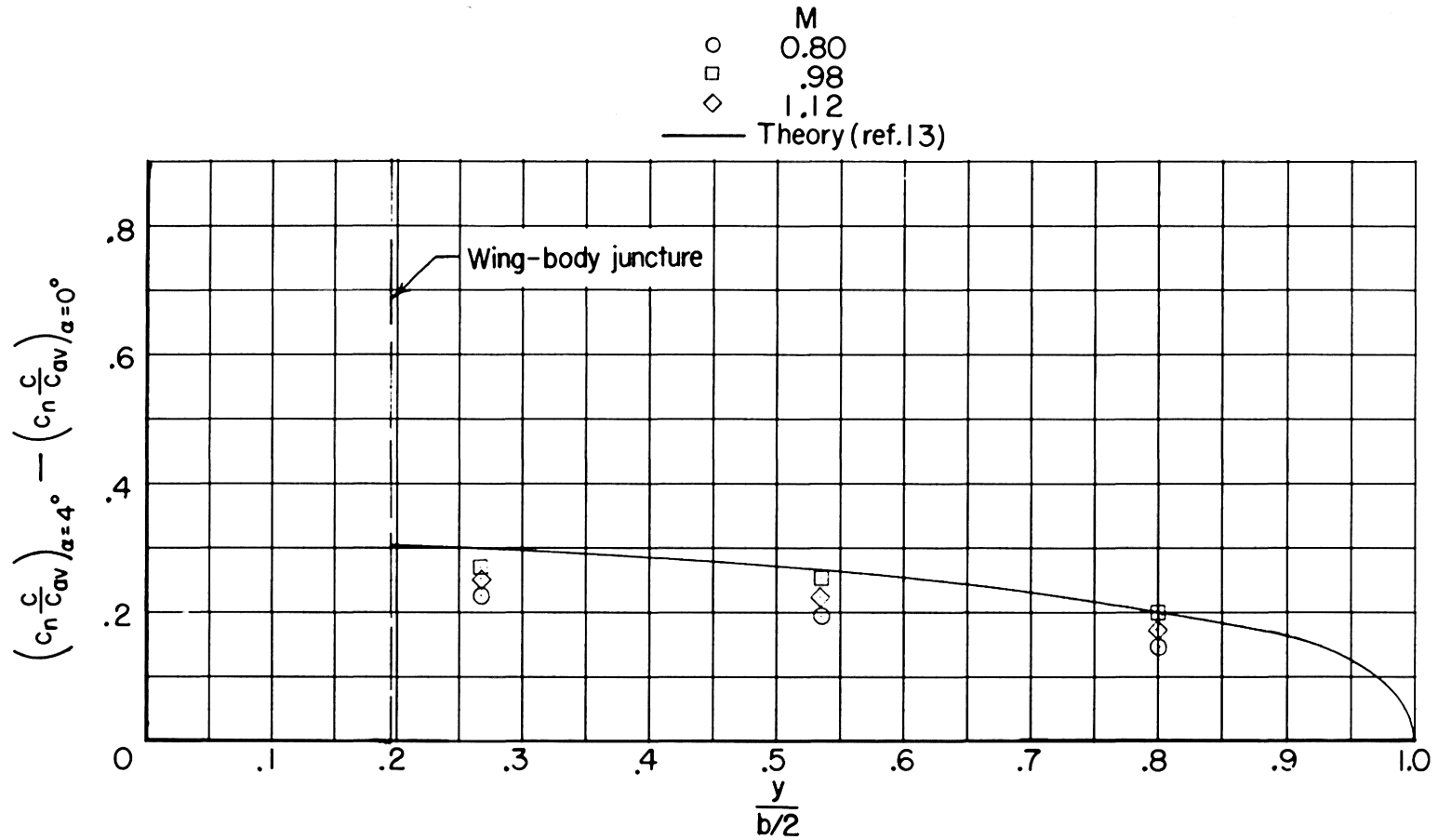


Figure 12.- Comparison of theoretical and experimental results.



CONFIDENTIAL

- 57 -

data is presented for the basic body configuration at three representative Mach numbers. The comparison is poor at Mach numbers of 0.80 and 1.12 but better at  $M = 0.98$ . Reference 13 indicates that the span loadings for a slender configuration are independent of Mach number. The dependence of the experimental span loadings on Mach number implies that this configuration is not slender from a theoretical standpoint. Reference 13 goes on to point out that at sonic velocity the term  $(1 - M^2)$  in the Prandtl linearized differential equation for the perturbation velocity potential is zero, and the equation again reduces to a two dimensional one, just as in the case of a slender configuration. In effect at sonic velocity the restriction that the configuration be slender is relaxed. The experimental data seems to verify the assumptions as shown by the better agreement at  $M = 0.98$ .

CONFIDENTIAL

CONFIDENTIAL

- 58 -

XI. CONCLUSIONS

An investigation to determine the aerodynamic loading characteristics of a thin low-aspect-ratio conical cambered delta wing-body combination has been conducted in the Langley 8-foot transonic tunnels. The data have been analyzed and indicate the following conclusions:

1. At subsonic speeds and at moderate angles of attack a leading-edge separation vortex causes the span load distributions to deviate from their approximately elliptical shape and approach triangular at the highest angles tested. The effect of this vortex is not as prominent at the higher Mach numbers.

2. Significant rearward and outboard center of pressure movements are noted at transonic speeds. Also some forward and inboard movements are noted at subsonic speeds at high normal force coefficients.

3. The effects of body indentation on the aerodynamic loading characteristics are small.

4. Comparison with experimental data for a similar plane wing indicates that the cambered wing is much more effective in utilizing the leading edge suction pressures to produce leading edge thrust. With increases in Mach number the benefit due to camber diminishes.

5. Theoretical and experimental results compared poorly at subsonic and low supersonic speeds. Better agreement was noted around sonic speeds.

CONFIDENTIAL

CONFIDENTIAL

- 59 -

## XII. SUMMARY

An investigation was conducted in the Langley 8-foot transonic tunnels to determine the aerodynamic loading characteristics of a thin conical cambered low-aspect-ratio delta wing in combination with a basic Sears-Haack Body and a body indented symmetrically for a Mach number of 1.2. The tests were conducted at Mach numbers from 0.60 to 1.12 and at 1.43 and at angles of attack from  $-4^{\circ}$  to  $20^{\circ}$ . The wing had an aspect ratio of 2.31 and had NACA 65A003 airfoil sections parallel to the model plane of symmetry over the uncambered portion.

The results indicate that a leading-edge separation vortex causes the shape of the span load distributions to change at moderate angles of attack. Significant transonic center of pressure movements are noted. Body indentation had little effect on the aerodynamic loading characteristics. Comparisons with experimental data for a similar plane wing indicates that the cambered wing is considerably more effective in utilizing the leading edge suction. Comparisons between experimental and theoretical results indicate fair agreement at sonic speeds.

CONFIDENTIAL

CONFIDENTIAL

- 60 -

### XIII. ACKNOWLEDGEMENTS

The author wishes to express his appreciation to the National Advisory Committee for Aeronautics for the opportunity to use material in this thesis which was obtained from a research project conducted at their Langley Laboratory.

He also wishes to thank Assistant Professor A. C. Bruce of the Aeronautical Engineering Department of the Virginia Polytechnic Institute for his advice and assistance in preparing this thesis.

CONFIDENTIAL

CONFIDENTIAL

- 61 -

XIV. REFERENCES

1. Jones, Robert T., Properties of Low-Aspect-Ratio Pointed Wings at Speeds Below and Above the Speed of Sound. NACA Rep. 835, 1946.
2. Mugler, John P., Jr., Effects of Two Leading-Edge Modifications on the Aerodynamic Characteristics of a Thin Low-Aspect-Ratio Delta Wing at Transonic Speeds. NACA RM L56G12a, 1956.
3. Mugler, John P., Jr., Transonic Wind-Tunnel Investigation of the Aerodynamic Loading Characteristics of a 60° Delta Wing in the Presence of a Body With and Without Indentation. NACA RM L55G11, 1955.
4. Hall, Charles F., Lift, Drag, and Pitching Moment of Low-Aspect-Ratio Wings at Subsonic and Supersonic Speeds. NACA RM A53A30, 1953.
5. Burrows, Dale L. and Palmer, William E., A Transonic Wind-Tunnel Investigation of the Longitudinal Force and Moment Characteristics of a Plane and a Cambered 3-Percent-Thick Delta Wing of Aspect Ratio 3 on a Slender Body. NACA RM L54H25, 1954.
6. Saltzman, Edwin J., Bellman, Donald R., and Musialowski, Norman T., Flight-Determined Transonic Lift and Drag Characteristics of the YF-102 Airplane With Two Wing Configurations. NACA RM H56E08, 1956.
7. Mugler, John P., Jr., Pressure Measurements at Transonic and Low Supersonic Speeds on a Thin Conical Cambered Low-Aspect-Ratio Delta Wing in Combination With Basic and Indented Bodies. NACA RM L57G19, 1957.
8. Ritchie, Virgil S. and Pearson, Albin O., Calibration of the Slotted Test Section of the Langley 8-Foot Transonic Tunnel and Preliminary Experimental Investigation of Boundary-Reflected Disturbances. NACA RM L51K14, 1951.
9. Matthews, Clarence W., An Investigation of the Adaptation of a Transonic Slotted Tunnel to Supersonic Operation by Enclosing the Slots With Fairings. NACA RM L55H15, 1955.
10. Hall, Charles F. and Heitmeyer, John Charles, Lift, Drag and Pitching Moment of Low-Aspect-Ratio Wings at Subsonic and Supersonic S; Speeds - Twisted and Cambered Triangular Wing of Aspect Ratio 2 With NACA 0003-63 Thickness Distribution. NACA RM A51E01, 1951.

CONFIDENTIAL

CONFIDENTIAL

- 62 -

11. Burnett, H. R., Geometry of Cambered Leading Edges and Warped Tips to be Evaluated in the NACA 8-Foot Tunnels for the F-102 Airplane. Aero. Memo. A-8-44 (Contract no. AF33(600)-5942), Consolidated Vultee Aircraft Corp., May 27, 1953.
12. Whitcomb, Richard T. and Fischetti, Thomas L., Development of a Supersonic Area Rule and an Application to the Design of a Wing-Body Combination Having High Lift-to-Drag Ratios. NACA RM L53H31a, 1953.
13. Spreiter, John R., The Aerodynamic Forces on Slender Plane- and Cruciform-Wing and Body Combinations. NACA Rep. 962, 1950.
14. Swihart, John M. and Foss, Willard E., Jr., Transonic Loads Characteristics of a 3-Percent-Thick 60° Delta-Wing-Body Combination. NACA RM L57D12, 1957.

CONFIDENTIAL

**The vita has been removed from  
the scanned document**

CONFIDENTIAL

ANALYSIS OF PRESSURE DATA OBTAINED AT TRANSONIC  
SPEEDS ON A THIN LOW-ASPECT-RATIO CAMBERED  
DELTA WING-BODY COMBINATION

By John P. Mugler, Jr.

ABSTRACT

An investigation was conducted in the Langley 8-foot transonic tunnels to determine the aerodynamic loading characteristics of a thin conical cambered low-aspect-ratio delta wing in combination with a basic body and a body indented symmetrically for a Mach number of 1.2 in accordance with the supersonic area rule. The tests were conducted at Mach numbers from 0.60 to 1.12 and at 1.43 and at angles of attack generally from  $-4^{\circ}$  to  $20^{\circ}$ . The wing was conically cambered over the outboard 15 percent of each semispan. The wing had an aspect ratio of 2.31,  $60^{\circ}$  sweepback of the leading edge, and had NACA 65A003 airfoil sections parallel to the model plane of symmetry over the uncambered portion.

The results of this investigation indicate that a leading-edge separation vortex forms at moderate angles of attack and causes the shape of the span load distribution to change markedly. Significant center of pressure movements are noted at transonic speeds. Indenting the body in accordance with the supersonic area rule had little effect

CONFIDENTIAL



CONFIDENTIAL

on the aerodynamic loading characteristics. Comparisons with experimental data for a similar plane wing indicates that the cambered wing is considerably more effective than the plane wing in utilizing the leading edge suction forces to produce thrust. A comparison between experimental and theoretical results indicates fair agreement around sonic speeds.

CONFIDENTIAL